

Direct measurement of the  $\bar{K}N \rightarrow \pi\Sigma$  scattering amplitude below the  $\bar{K}N$  threshold employing the  $d(K^-, N)\pi\Sigma^-$  reaction

Kentaro Inoue

February 1, 2025

# Contents

<b>1</b>	<b>Introduction</b>	<b>3</b>
1.1	$\Lambda(1405)$ and $\bar{K}N$ interaction . . . . .	3
1.2	$d(K^-, n)$ reaction . . . . .	6
1.3	The J-PARC E31 experiment . . . . .	7
<b>2</b>	<b>Experimental setup</b>	<b>12</b>
<b>3</b>	<b>Analysis</b>	<b>13</b>
<b>4</b>	<b>Discussion</b>	<b>14</b>
4.1	Decomposition of the $K^-d \rightarrow n\pi^+\pi^-n$ events . . . . .	14
4.1.1	Backward $\pi^\mp\Sigma^\pm$ event selection . . . . .	14
4.1.2	Template fitting . . . . .	16
4.2	Conversion to the cross section . . . . .	23
4.3	Spectra . . . . .	28
4.3.1	Qualitative properties of obtained spectra . . . . .	28
4.3.2	Comparison with theoretical calculations . . . . .	29
4.3.3	$\bar{K}N$ Pole parameters assuming the 2-step reaction .	31
4.3.4	Comparison with DCC model . . . . .	38
<b>5</b>	<b>Conclusion</b>	<b>44</b>
<b>A</b>	<b><math>\pi^0\Sigma^0</math> spectrum analysis</b>	<b>45</b>
<b>B</b>	<b>Detector resolution</b>	<b>46</b>
B.1	CDC resolution . . . . .	46
B.2	Detector resolution on the $d(K^-, N)$ . . . . .	46
<b>C</b>	<b><math>d(K^-, n)K^0n</math> analysis</b>	<b>47</b>

# Chapter 1

## Introduction

### 1.1 $\Lambda(1405)$ and $\bar{K}N$ interaction

The  $\Lambda(1405)$  is a hyperon with strangeness  $S = -1$ , isospin  $I = 0$  and spin and spin parity  $J^P = (\frac{1}{2})^-$ . In the latest Particle Data Group (PDG) [1], the mass and the width of the  $\Lambda(1405)$  are assigned to  $1405.1_{-1.0}^{+1.3}\text{MeV}$  and  $50.5 \pm 2.0\text{MeV}$  respectively, based on several papers [2–4].

The existence of the  $\Lambda(1405)$  was predicted for the first time by R. H. Dalitz and S. F. Taun in 1959 as a quasi-bound state of  $\bar{K}N$  [5]. The candidate was reported to have been found in the  $K^-p \rightarrow \pi\pi\pi\Sigma$  reaction at the Lawrence Radiation Laboratory in 1961 [6]. The excess was reported in the neutral  $\pi\Sigma$  spectrum,  $K^-p \rightarrow \pi^\pm\pi^\mp(\pi\Sigma)^0$ , in the  $\Lambda(1405)$  region compared to the doubly charged spectrum,  $K^-p \rightarrow \pi^+\pi^+(\pi^-\Sigma^-)$  or  $K^-p \rightarrow \pi^-\pi^-(\pi^+\Sigma^+)$ , in this paper. However, there was not enough statistical data to discuss lineshape. There was also the problem of ambiguity about where each  $\pi$  came from.

In order to solve these problems, R. J. Hemingwey reported high-statistics  $\pi^+\Sigma^-$  and  $\pi^-\Sigma^+$  spectra using the  $K^-p \rightarrow \pi^-\Sigma^+(1660) \rightarrow \pi^-\pi^+(\pi^\mp\Sigma^\pm)$  with 4.2 GeV/c  $K^-$  beam [7]. In these spectra, the momentum transfer was restricted to,  $t(K^-, \pi^-) < 1.0$  GeV/c, in order to increase the purity of  $\Sigma^+(1660)$ . As a result, the  $\Sigma^+ \rightarrow \pi^0 p$  decay event of the  $K^-p \rightarrow \pi^-\Sigma^+(1660) \rightarrow \pi^-\pi^+(\pi^-\Sigma^+)$  reaction gave a  $\pi^-\Sigma^+$  spectrum with almost no background. R. H. Dalitz and A. Deloff obtained the mass and width of the  $\Lambda(1405)$  as  $1406.4 \pm 4.0$  MeV and  $50 \pm 2$  MeV [2] by adapting the M-matrix method to this spectrum, and these parameters were adopted for the PDG. On the other hand, the  $\pi^+\Sigma^-$  spectrum of the  $K^-p \rightarrow \pi^-\Sigma^+(1660) \rightarrow \pi^-\pi^+(\pi^+\Sigma^-)$  reaction had a background due to the ambiguity of the origin

of the  $\pi^-$ .

Considering the  $\Lambda(1405)$  as a  $\bar{K}N$  bound state, the  $\bar{K}N$  interaction should be attractive. From the 1960's to the 1980's, various  $K^-p \rightarrow$  meson-baryon, e.g.,  $K^-p$ ,  $K^0n$ ,  $\pi\Lambda$ ,  $\pi\Sigma$ , and so on, scattering data were measured on hydrogen target using bubble chambers to study the  $\bar{K}N$  interaction [8–12]. This method of course did not allow access below the  $\bar{K}N$  threshold and measurements in the low energy region were difficult and data were not enough. Nevertheless, the value of the  $\bar{K}N$  interaction at the  $\bar{K}N$  threshold was obtained by exterior it from the high energy region, where there is abundant data, using several models [13–15]. Due to the lack of data in the low energy region, these values varied. However, they were all attractive and consistent with the  $\Lambda(1405)$  being a  $\bar{K}N$  bound state.

A direct measurement of the  $\bar{K}N$  interaction at the  $\bar{K}N$  threshold was attempted by binding a  $K^-$  meson to a hydrogen atom instead of an electron and measuring the characteristic  $X$ -ray shift. Around 1980, experiments with liquid hydrogen reported a positive shift, implying that the  $\bar{K}N$  interaction is repulsive [16–18]. This result was inconsistent with  $\bar{K}N$  scattering experiments, which regarded the  $\bar{K}N$  interaction as an attractive force.

Iwasaki et al. pointed out that these experiments showed a poor signal-to-noise ratio in the region of interest where the energy shift is below zero. To remedy this problem, they performed an experiment using a gaseous hydrogen target at KEK-PS [19] and found a negative energy shift peak and concluded that the  $I = 0$   $\bar{K}N$  interaction is attractive. The experiment was updated to high precision by the SHIDDARTA collaboration [20] and its values were used as constraints to extrapolate  $\bar{K}N$  scattering amplitudes below the  $\bar{K}N$  threshold from  $\bar{K}N$  scattering experiments.

The conclusion that the  $\bar{K}N$  interaction is attractive accelerated theoretical analyses that consider the  $\Lambda(1405)$  as a  $\bar{K}N$  bound state. In this framework, the  $\Lambda(1405)$  is considered to be dynamically generated and decays to  $\pi\Sigma$  via the  $\bar{K}N$  channel. In this depiction, the Lagrangian includes strange sector with  $\bar{K}N$ ,  $\pi\Lambda$ ,  $\pi\Sigma$ ,  $\eta\Lambda$ ,  $\eta\Sigma$ , and  $K\Xi$  channels is used. The low-energy perturbation expansion of this Lagrangian was considered difficult to analysis near the  $\Lambda(1405)$  region. Therefore, the chiral unitary model was proposed to extend the effective region near the  $\Lambda(1405)$  by imposing unitary conditions on multi-channels in the strangeness sector, and a theoretical analysis was proceeded using this model.

J. C. Nacher et al. [21] calculated  $\pi\Sigma$  channels, i.e.  $\pi^+\Sigma^-$ ,  $\pi^0\Sigma^0$  and  $\pi^-\Sigma^+$  line shapes from photoproduction,  $\gamma p \rightarrow K^+\Lambda(1405)$ , using the chiral unitary model. They showed that the  $\pi\Sigma$  spectra differs depending on the charge mode and argued that the difference reflects the nature of  $\Lambda(1405)$ .

This suggests that not only the  $I = 0$   $\bar{K}N$  interaction but also the  $I = 1$   $\bar{K}N$  interaction affects the  $\pi\Sigma$  spectra.

M. Niiyama et al. experimentally measured  $\pi^+\Sigma^-$  and  $\pi^-\Sigma^+$  spectra caused by photoproduction at LEPS [22]. They measured  $\gamma p \rightarrow K^+(\pi^\pm\Sigma^\mp)$  spectra by detecting forward-scattered  $K^+$  at  $0.8 < \theta_{K^+}$  using a  $\gamma$ -ray beam of  $E_\gamma = 1.5\text{-}2.4$  GeV. They reported differences in their spectra below the  $\bar{K}N$  threshold and showed the presence of  $I = 0$  and  $I = 1$  interference terms in  $\Lambda(1405)$ . The CLAS collaboration reported spectra of all three  $\pi\Sigma$  channels, with high statistical data on photoproduction [23, 24]. They measured the forward-scattered  $K^+$ ,  $0.6 < \Theta_{K^+} < 0.9$ , using a  $\gamma$ -ray beam of  $E_\gamma = 1.61\text{-}1.91$  GeV. The spectra show large differences at vicinity of the  $\Lambda(1405)$ , suggesting more strongly the presence of  $I = 1$  and interference term effects in this region. Although this spectra did not agree with the calculations by J.C.Nacher et. al. [21], it was shown by S.X.Nakamura and D.Jido that the spectra is reproduced by a gauge-invariant photoproduction mechanism using a chiral unitary model in which many parameters are introduced [25]. The fact that many parameters are introduced here means that the reaction mechanism is complex and there is interference of  $I = 0$  and  $I = 1$  between some parameters.

D.Jido et al. proposed that  $\Lambda(1405)$  is influenced by two poles strongly coupled to  $\bar{K}N$  and  $\pi\Sigma$ , respectively, through a detailed theoretical analysis using the chiral unitary model [26]. According to this depiction, the  $\bar{K}N$  pole appears above the conventional 1.405 GeV and the  $\pi\Sigma$  pole appears below 1405 MeV. The HADES collaboration performed  $\Lambda(1405)$  production experiments using  $pp$  collisions, a different reaction mechanism to photoproduction [27]. They reported  $(\pi^\pm\Sigma^\mp)$  spectra from the  $pp \rightarrow K^+p(\pi^\pm\Sigma^\mp)$  reaction using a proton beam with an energy of 3.5 GeV. The peak of the spectrum clearly appeared below 1.4 GeV. Thus, it was found that the spectrum of  $\Lambda(1405)$  depends on the reaction mechanism and the  $\pi\Sigma$  channel, which reinforces the depiction that  $\Lambda(1405)$  is a dynamically generated meson baryon state and promotes analysis according to this depiction.

Y. Ikeda et al. [28] and Z.-H. Geo et al. [29] improved the analysis of the chiral unitary model by constraining the  $\bar{K}N$  interaction at the  $\bar{K}N$  threshold from the  $X$ -ray shift by SHIDDARTA and reported the scattering amplitude for the  $\bar{K}N$  interaction and the parameters for the  $\Lambda(1405)$ . M. Mai et al. analysed in a similar way and obtained several solutions. Finally, they reporting two parameters for the  $\Lambda(1405)$  and the scattering amplitude for the  $\bar{K}N$  interaction by sieving by  $\pi\Sigma$  spectra by CLAS photoproduction [30].

For the higher energy regions, detailed partial-wave analyses have been

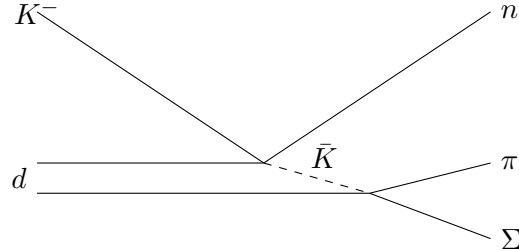


Figure 1.1: The diagram of 2step  $K^-d \rightarrow n\pi\Sigma$  reaction.

carried out because of the large amount of scattering data available, as mentioned above, and many excited states of hyperons have been predicted, and many of them have been experimentally confirmed. The most recent static partial wave analysis was performed by a group at Kent State University (KSU) [31, 32]. However, in that analysis,  $\Lambda(1405)$  was fixed to the value by PDG and the structure of  $\Lambda(1405)$  could not be discussed. Kamano et al. reported the results of analysing the structure of dynamically generated  $\Lambda(1405)$  by adapting the Dynamical Coupled Channel method, which extends partial wave analysis to dynamics, to strange sectors containing such as  $K$ ,  $\Lambda$ ,  $\Sigma$  and so on [33]. Although there were two DCC models due to shortage of data in the low momentum region, both models had two  $I = 0$  poles below the  $\bar{K}N$  threshold as in the chiral unitary model, with the higher pole strongly coupled to  $\bar{K}N$  and the lower pole to  $\pi\Sigma$ . However, the position and width of these poles differed significantly between the two models.

## 1.2 $d(K^-, n)$ reaction

As mentioned above,  $\Lambda(1405)$  is closely related to the  $\bar{K}N$  interaction and scattering data below the  $\bar{K}N$  threshold of Kaon and nucleon are desired, but cannot be scattered directly in free space due to energy conservation laws. By using a deuterium target, the irradiated Kaon beam is scattered by one nucleon, which energises the nucleon and becomes a virtual  $\bar{K}$ . The virtual  $\bar{K}$  reacts with the residual nucleon and becomes  $\pi\Sigma$ . The diagram of this reaction is shown in Figure 1.1. By flying the virtual  $\bar{K}$  to intermediate states, information below the  $\bar{K}N$  threshold can be accessed.

An experiment to measure the  $\pi Y$  spectrum from  $Y^*$  produced by irradiating liquid deuterium with a  $K^-$  beam at a momentum of 686-848 MeV/ $c$

was performed at CERN by Braun et al. by a bubble chamber [34]. They only reported  $K^-d \rightarrow n(\pi^+\Sigma^-)$  spectra as information containing  $I = 0$ . They also reported another pure  $I = 1$  spectrum,  $K^-d \rightarrow p(\pi^-\Lambda)$ . It is well known that the  $p$ -wave scattering,  $\Sigma(1385)$ , is present in the  $I = 1$  channel below the  $\bar{K}N$  threshold. They estimated the influence of  $\Sigma(1385)$  from the  $\pi^-\Lambda$  spectrum and confirmed that its effect on the  $\pi^+\Sigma^-$  spectrum is small.

The peak position of the  $\pi^+\Sigma^-$  spectrum was clearly located in a region higher than the conventional 1405 MeV. Jido et al. showed that if this reaction is considered within the framework of the chiral unitary model, the influence of the  $\bar{K}N$  poles is dominant and the peak position is around 1420 MeV, reproducing the experimental spectrum of  $K^-d \rightarrow n(\pi^+\Sigma^-)$  [35]. In the same framework, Yamagata et al. calculated an  $I = 1$   $\pi^-\Lambda$  spectrum incorporating  $\Sigma(1385)$  and confirmed that it reproduced the experimental spectrum [36]. They estimated the influence of  $\Sigma(1385)$  in the framework of this theoretical calculation and confirmed that the influence on the  $\pi^+\Sigma^-$  spectrum was small.

However, they did not report a  $\pi^-\Sigma^+$  spectrum and therefore could not discuss the influence of  $I = 0$  and  $I = 1$  interference on this reaction. They were also unable to discuss detailed kinematic factors because of the low momentum of the  $K^-$  beam and all the angles of the scattered nucleons were summarised.

The J-PARC E31 experiment was planned and performed to solve these problems [37]. The next subsection provides an overview of the J-PARC E31 experiment and the physics discussed in this paper.

### 1.3 The J-PARC E31 experiment

In the J-PARC E31 experiment, a liquid deuterium target is irradiated with a 1.0 GeV/c  $K^-$  beam to measure kinetics, which are identified by detecting super-forward scattered nucleons  $\theta_n = 0$  degree. In this kinematics, the virtual  $\bar{K}$  is recoiled backwards and reacts with residual nucleons to become  $\pi\Sigma$ . The mass of  $\pi\Sigma$  is measured by the  $d(K^-, N)$  missing mass method and the charge state of  $\pi\Sigma$  is identified by measuring charged particles due to decay in a cylindrical detector system (CDS) placed around a liquid deuterium target.

After the J-PARC E31 experiment was proposed, a spectrum was calculated for the kinematics of the experiment based on several theories. It was argued by K. Miyagawa et al. [38] that  $\Lambda(1405)$  is due to  $\bar{K}N$  scattering in the low energy region and data from that region should be used for

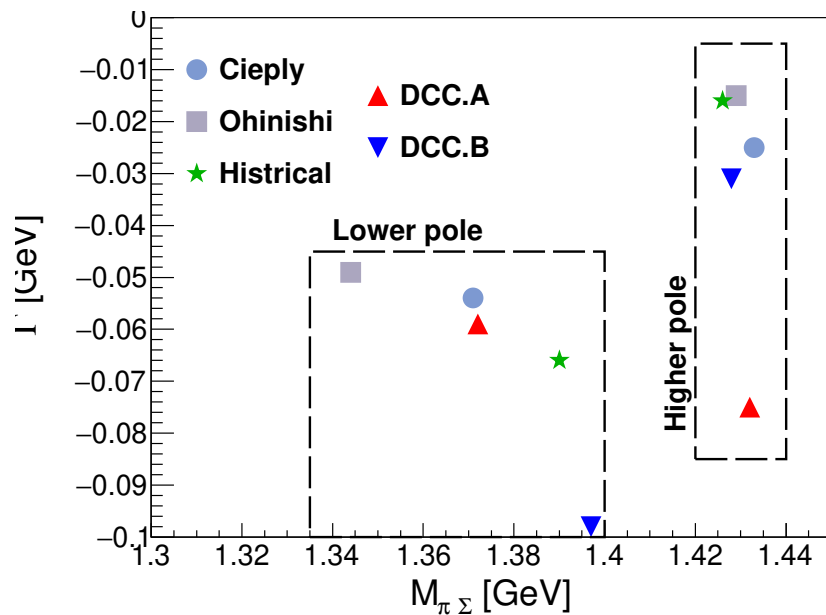


Figure 1.2: This figure shows the pole structure with  $I = 0$   $\bar{K}N$  scattering amplitudes below the  $\bar{K}N$  threshold used in the theoretical calculation of the predicted spectrum of the E31 experiment.

the second step scattering, while the J-PARC E31 experiment uses a high momentum  $K^-$  beam of 1.0 GeV/ $c$ , so  $\bar{K}N$  scattering data from the high energy region should be used. They used scattering amplitudes from the partial wave analysis by the KSU group presented in Section 1.1 for the first scattering in the high energy region, and scattering amplitudes from the three chiral analyses for the  $\bar{K}N$  scattering data in the low energy region of interest. One is from E. Oset et al. in the early period when chiral analysis was proposed [39], and the other two are from A. Cieplý et al. [40] and S. Ohnishi et al. [41] after the SIDDARTA result was presented. These two are imposed the constrain to the  $\bar{K}N$  scattering amplitude by the  $\bar{K}N$  scattering length from the kaonic hydrogen by SIDDARTA.

Also, theoretical spectra calculated by the DCC method introduced in Section 1.1 have also been reported by H. Kamano et al. [42]. The DCC method covers a wide region from the low-energy  $\bar{K}N$  bound region of  $\Lambda(1405)$  to the high-energy  $\bar{K}N$  scattering of the first scattering of this reaction with continuous scattering amplitudes, which is used in this calculation. There are two models for the DCC method, both of which have two poles but their positions are significantly different.

The pole structure of the  $I = 0$  poles below the  $\bar{K}N$  threshold, i.e.  $\Lambda(1405)$ , used in these theoretical calculations is shown in Fig.1.2. All models have two poles, but their values vary widely from model to model.

Assuming a two-step reaction as described above, Noumi et. el. [43] focused on the second step of  $\bar{K}N \rightarrow \pi\Sigma$  scattering and performed a fit using the scattering length and effective range, which are complex numbers, as free parameters. As a result, we obtained the values  $A = [-1.12 \pm 0.11(fit)^{+0.10}_{-0.07}(syst.)] + [0.84 \pm 0.12(fit)^{+0.08}_{-0.07}(syst.)]$  fm and  $R = [-0.18 \pm 0.32(fit)^{+0.08}_{-0.06}(syst.)] + [-0.40 \pm 0.13(fit) \pm 0.09(syst.)]$  fm for the scatter length and effective range resulting in Figure.1.3. From those values, the pole positon and width of  $\Lambda(1405)$  are obtained as  $1417.7^{+6.0}_{-7.4}(fit)^{+1.1}_{-1.0}(syst.)$  MeV/ $c^2$  and  $26.1^{+6.0}_{-7.9}(fit)^{+1.7}_{-2.0}(syst.)$  MeV/ $c^2$ . The scattering length and effective range are the first-order and second-order parameters in the low-energy expansion of the two-channel scattering between  $\bar{K}N$  and  $\pi\Sigma$ . In that figure, the spectrum obtained from the experiment is depicted in the above panel, and the  $\bar{K}N \rightarrow \bar{K}N$  scattering amplitudes for  $I = 0$  obtained from the fit are depicted in the lower panel. In the above panel, the black error bars in the above figure are the spectra obtained from the  $\Sigma^+\pi^-$  and  $\Sigma^-\pi^+$  spectra with  $I = 0$  and 1 and their interference terms, and the  $\Sigma^-\pi^0$  spectrum with  $I = 1$ . The blue error bar is the  $\Sigma^0\pi^0$  spectrum with  $I = 0$ . The spectra obtained from the fit are depicted by the red lines, where the

dashed lines do not include the detector resolution and the solid lines are convolved with the resolution. The estimation of the resolution is described in detail in Appendix.???. In the lower panel, the real and imaginary parts of the  $\bar{K}N \rightarrow \bar{K}N$  scattering amplitude obtained from the fit are shown as black and red lines, respectively. The real and imaginary parts of the scattering amplitudes are represented by the black and red lines, respectively, in the down figure. The green and blue vertical lines represent the  $\bar{K}N$  threshold and the pole position of  $\Lambda(1405)$ , respectively. These analyses are described in detail in Section.4.3.3.

In this paper, detailed measurements and analysis methods for the  $\pi^-\Sigma^+$ ,  $\pi^+\Sigma^-$ , and  $\pi^-\Sigma^0$  spectra measured in the J-PARC E31 experiment are explained. The  $\pi^-\Sigma^+$  and  $\pi^-\Sigma^-$  spectra have contributions from  $I = 0$ ,  $I = 1$ , and their interference terms, while  $\pi^-\Sigma^0$  only contributes from pure  $I = 1$ . From these three spectra, we discuss the respective contributions by decomposing them into  $I = 0$ ,  $I = 1$ , and their interference terms, and comparing them with the spectra predicted from the theory introduced earlier. The  $\pi^0\Sigma^0$  spectrum shown in Figure. 1.3 is described in detail in the paper by S. Kawasaki [44], and a summary is given in the Appendix A.

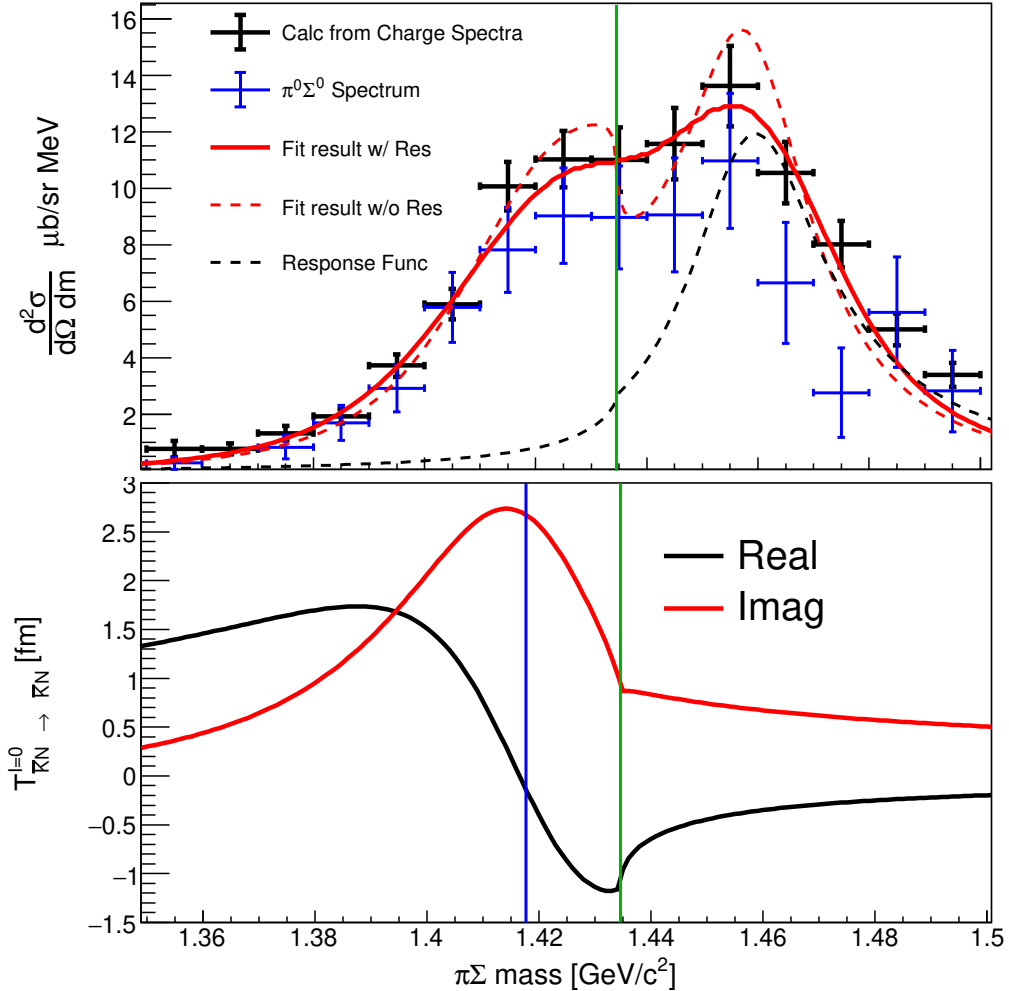


Figure 1.3: This picture shows the result of fitting the spectrum with E31 by Noumi et al []. The error bars in the upper panel represent experimental data, with black representing the  $I = 0$  spectrum calculated from  $\pi^-\Sigma^+$ ,  $\pi^+\Sigma^-$  and  $\pi^0\Sigma^-$ , and blue representing the  $\pi^0\Sigma^0$  spectrum with  $I = 0$ . The solid red line is the result of a fit assuming a two-step reaction, solid and dashed represents with and without detector resolution. The lower panels show the scattering amplitude of the second step  $\bar{K}N \rightarrow \bar{K}N$  scattering obtained by the fitting, where the black and red lines represent the real and imaginary parts, respectively. The vertical green and blue lines represents  $\bar{K}N$  threshold and pole position of  $\Lambda(1405)$ , respectively.

# **Chapter 2**

## **Experimental setup**

## Chapter 3

# Analysis

# Chapter 4

## Discussion

### 4.1 Decomposition of the $K^-d \rightarrow n\pi^+\pi^-n$ events

#### 4.1.1 Backward $\pi^\mp\Sigma^\pm$ event selection

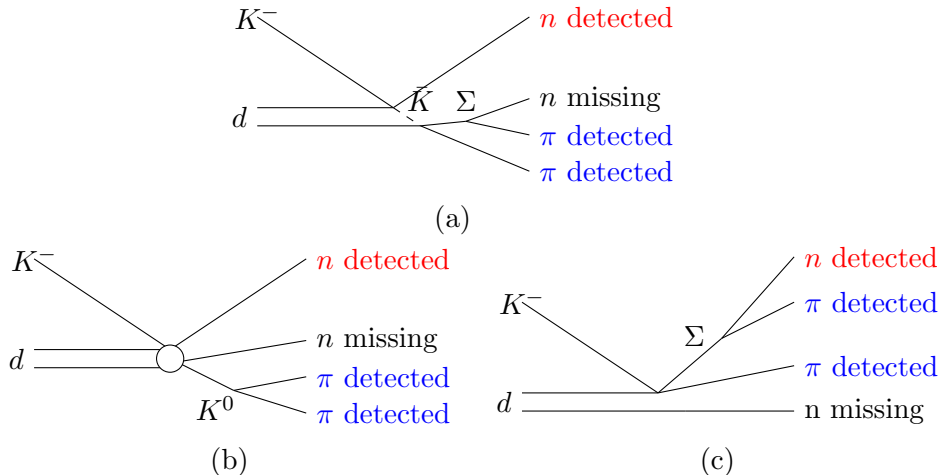


Figure 4.1: These figures illustrate the reaction diagrams of this final state. (a) shows backward  $\pi\Sigma$  scattering via virtual  $\bar{K}$ ; (b) depicts direct decay from real  $K^0$  to  $\pi^+\pi^-$ ; (c) indicates forward  $\Sigma$  production. Colored particles indicate that a particle was detected. Red and blue mean detection by the NC and the CDS, respectively.

The  $K^-n \rightarrow n\pi^+\pi^-n$  final state is identified from the event in which the forward neutron is detected, as described in Section.???. This final state can

be considered to include the three reactions represented in Figure 4.1. The first is the signal reaction in this analysis where  $\bar{K}$  is recoiled backward to  $\pi\Sigma$  as shown in Figure 4.1-(a), the second is the recoiled  $K^0$  decaying directly to  $\pi^+\pi^-$  as shown in Figure 4.1-(b), and the third is the forward production of  $\Sigma$  ( $\Sigma_{forward}$ ) as shown in Figure 4.1-(c), where forward means that the  $n$  decaying from  $\Sigma$  are detected by the NC. Reactions (b) and (c) can be identified by reconstructing  $K^0$  and  $\Sigma^\pm$  from the invariant masses of  $\pi^+$  and  $\pi^-$  and forward neutrons and  $\pi^\pm$ , respectively, as shown in Figure 4.2. The invariant mass distributions of  $\pi^+\pi^-$ ,  $n\pi^-$  and  $n\pi^+$  are represented in the right, center and left figures respectively. For the identification of  $K^0$  and  $\Sigma_{forward}^\pm$ , fitting with third polynomial function and Gaussian function is used to identify  $K^0$  and  $\Sigma_{forward}^\pm$  in the  $3\sigma$  region of the Gaussian function, which indicated by the red hatched area.

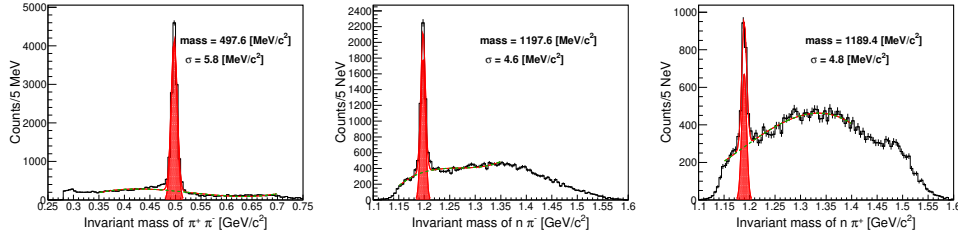


Figure 4.2: These figures show the invariant mass distributions of  $\pi^+\pi^-$ ,  $n\pi^-$  and  $n\pi^+$  in the  $Kd \rightarrow n\pi^+\pi^-n$  event sample from left to right. The Gaussian functions and regions for  $K^0$  and  $\Sigma_{forward}^\pm$  selection are represented by red hatches. The background third-degree polynomial functions are represented by the green dashed lines.

Rejecting these two reactions leaves a signal reaction in which  $\pi\Sigma$  is scattered backward. This reaction has  $\pi^-\Sigma^+$  and  $\pi^+\Sigma^-$  modes, which must be separated. The branching ratio of these modes depends on the mass of  $\pi\Sigma$ , and this is done for each bin of  $d(K^-, n)$  missing mass.

Figure 4.3 shows the  $d(K^-, n)$  missing masses for which the  $K^-d \rightarrow n\pi^+\pi^-n$  end state has been identified. On the left, all events, those identifying  $K^0$ , those identifying  $\Sigma_{forward}^+$ , and those identifying  $\Sigma_{forward}^-$  are indicated by black, green, red, and blue lines, respectively. The right figure shows the spectrum of the signal, subtracting the events identified as  $K^0$  or  $\Sigma_{forward}^\pm$  from all events.

To separate these events, we generated template events using a Geant4 Monte Carlo simulation and decomposed the reactions by fitting their spectra with templates. This decomposition was applied not only to the signal

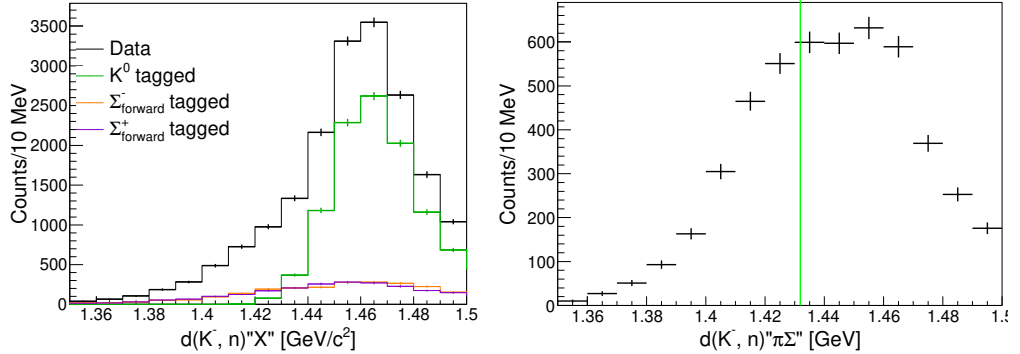


Figure 4.3: This figure shows the  $d(K-d)$  spectrum of the  $K^-d \rightarrow n\pi^+\pi^-n$  final state. All of the left figures are represented by  $K^0$  identified,  $\Sigma^+$  identified, and  $\Sigma^-$  identified in black, green, orange, and purple. Our signals scattered  $\pi\Sigma$  backward are those other than those identified and they are represented in the right figure.

but also to the background reactions, the procedures used in this decomposition, which are described in detail in Section 4.1.2. The estimation of the detector resolution used in this simulation is described in detail in Appendix B.

#### 4.1.2 Template fitting

This subsection describes template fitting for reaction decomposition. Earlier, three possible reactions in the  $K^-d \rightarrow n\pi^+\pi^-n$  final state were mentioned. Among them, backward  $\pi\Sigma$  scattering (Figure 4.1-(a)) and forward  $\pi\Sigma$  production (Figure 4.1-(c)) can be divided into two categories depending on the charge state of  $\pi\Sigma$ . In other words, template events were generated for these five reactions.

1.  $K^-d \rightarrow n_{forward}\pi^-\Sigma^+$  (Signal-1)
2.  $K^-d \rightarrow n_{forward}\pi^+\Sigma^-$  (Signal-2)
3.  $K^-d \rightarrow nK^0n$  ( $K^0$  production)
4.  $K^-d \rightarrow \Sigma^+\pi^-n$  ( $\Sigma^+_{forward}$  production)
5.  $K^-d \rightarrow \Sigma^-\pi^+n$  ( $\Sigma^-_{forward}$  production)

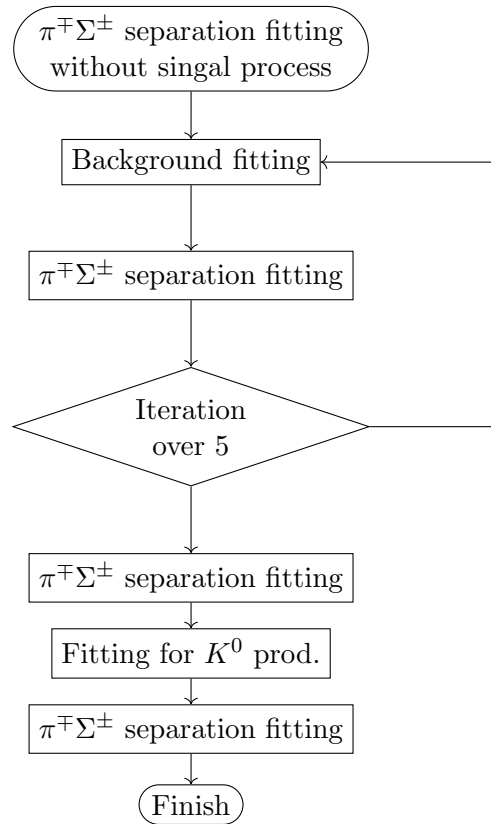


Figure 4.4: Flow chart of template fittings of this analysis.

Among these, reaction 3 is considered to be an elementary process in which the  $K^-$  kicks the proton in the deuteron forward as a neutron and recoils backward as a  $K^0$ . In this reaction, the other nucleon, the neutron, acts as a spectator with Fermi momentum. The Fermi momentum simulates the results of the  $d(e, e'p)n$  reaction [60]. In reactions 4 and 5, the  $\Sigma$  is scattered forward, meaning it is considered an elementary process because much of the momentum from the  $K^-$  beam is transferred to the  $\Sigma$  (and the  $\pi$ ). A lot of data on these elementary processes have been collected from scattering experiments using hydrogen targets, and their angular distributions are summarized in [59]. The angular distributions of reactions 3-5 simulate these processes.

These three reactions are considered to be the background in this analysis, and we need to generate template events for backward  $\pi\Sigma$  scattering (reactions 1 and 2), which represent the signal. However, no data are available for these reactions because they are 2-step reactions and the intermediate particle  $\bar{K}$  is a virtual particle. Additionally, the fitting for the mode separation of  $\pi^-\Sigma^+$  and  $\pi^+\Sigma^-$  is performed for each bin of the  $d(K^-, n)\pi\Sigma$  missing mass. Furthermore, these Monte Carlo samples are used for the acceptance correction as described in Section 4.2. Therefore, this template event was generated according to a uniform  $\pi\Sigma$  mass distribution. The second step scattering,  $\bar{K}N \rightarrow \pi\Sigma$  scattering, was produced isorotopically because  $\Lambda(1405)$  is  $S$ -wave.

Template fitting is divided into two tasks: background estimation and the separation of the  $\pi^-\Sigma^+$  and  $\pi^+\Sigma^-$  modes. The task for background estimation is performed using all  $K^-d \rightarrow n\pi^+\pi^-n$  final states. On the other hand, the task for the separation of the  $\pi\Sigma$  charged modes is carried out using background ( $K^0$  and  $\Sigma$  production) removed events, which are further categorized into each bin of the  $d(K^-, n)\pi\Sigma$  missing mass. In other words, these fittings cannot be performed simultaneously with the other because the events used are different. Thus, the fittings perform according to Figure 4.4. First, an initial fitting for  $\pi^\mp\Sigma^\pm$  separation is performed without considering the backgrounds. Next, background fitting is conducted to estimate the contribution from  $\pi^\mp\Sigma^\pm$ . Next, fitting for charge mode separation is performed, taking background leakage into account. These fittings are performed iteratively five times since the background and  $\pi\Sigma$  spectra affect each other. Since we found that the background of  $K^0$  production includes reactions that are not elementary processes, we finally perform a fitting using  $K^0$ -selected events to separate these contributions. This step is referred to as "Fitting for  $K^0$  production" in Figure 4.4 and is described in detail in Appendix C. The final spectrum is obtained by fitting the  $\pi^\mp\Sigma^\pm$  charge

mode separation one last time. In this fitting, the background is removed in the range of  $3\sigma$ , which means that the "fitting for  $K^0$  production" has almost no effect on the final result. These so-called template fittings are performed according to ROOT's TFractionFitter implemented according to "Fitting with Finite Monte Carlo Samples" [62].

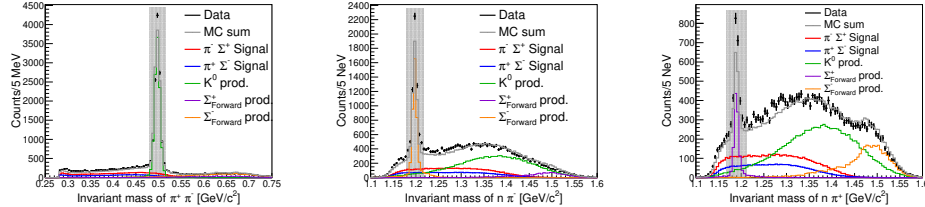


Figure 4.5: The figures show template fitting for background estimation. The right, center, and left figures show invariant masses of  $\pi^+\pi^-$ ,  $n\pi^-$  and  $n\pi^+$ , respectively. Error bars indicate data spectra. Bold lines indicate backward  $\pi\Sigma$  production signals, red and blue indicate  $\pi^-\Sigma^+$  and  $\pi^+\Sigma^-$ , respectively. The green, purple, and orange thin lines indicate the  $K^0$ ,  $\Sigma_{forward}^-$  and  $\Sigma_{forward}^+$  production reactions. Gray lines indicate the sum of MC simulations. Gray hatching indicates the  $3\sigma$  rejection region estimated by fitting with Gaussian and polynomial backgrounds.

Next, the fitting for background and  $\pi^\mp\Sigma^\pm$  separation is explained in detail. Background fitting is performed using the invariant mass spectra for  $\pi^+\pi^-$ ,  $n_{forward}\pi^+$ , and  $n_{forward}\pi^-$  with all  $K^-d \rightarrow n\pi^+\pi^-n$  final states shown in Figure 4.2. The contributions from each process, scaled by the fitting results, are presented in Figure 4.5.  $K^0$ ,  $\Sigma^+$ , and  $\Sigma^-$  production are represented by green, purple, and orange lines, respectively, creating peaks at the corresponding  $\pi^+\pi^-$ ,  $n_{forward}\pi^+$ , and  $n_{forward}\pi^-$  invariant masses. The backward  $\pi^-\Sigma^+$  and  $\pi^+\Sigma^-$  scattering signals are represented by red and blue lines, respectively, and are uniformly distributed without peaks at these invariant masses. The fact that these invariant mass distributions are reproduced from the template generated by the MC simulation indicates that the  $K^-d \rightarrow n\pi^+\pi^-n$  final state can be decomposed by the signal and  $K^0$  and  $\Sigma_{forward}^\pm$  production. In template fitting, it is known that  $-2\ln(\Lambda)$  asymptotes to the  $\chi^2$  in the limit of infinite number of samples, where  $\Lambda$  means likelihood. In this fitting,  $-2\ln(\Lambda)/NDF \sim \chi^2/NDF = 1077.4/352 = 3.06$ .

Next, we explain the fitting process to separate the  $\pi^-\Sigma^+$  and  $\pi^+\Sigma^-$  charge modes of the backward  $\pi\Sigma$  scattering which is the signal in this analysis. For this purpose, we use the missing masses of  $d(K^-, n\pi^-)$  and

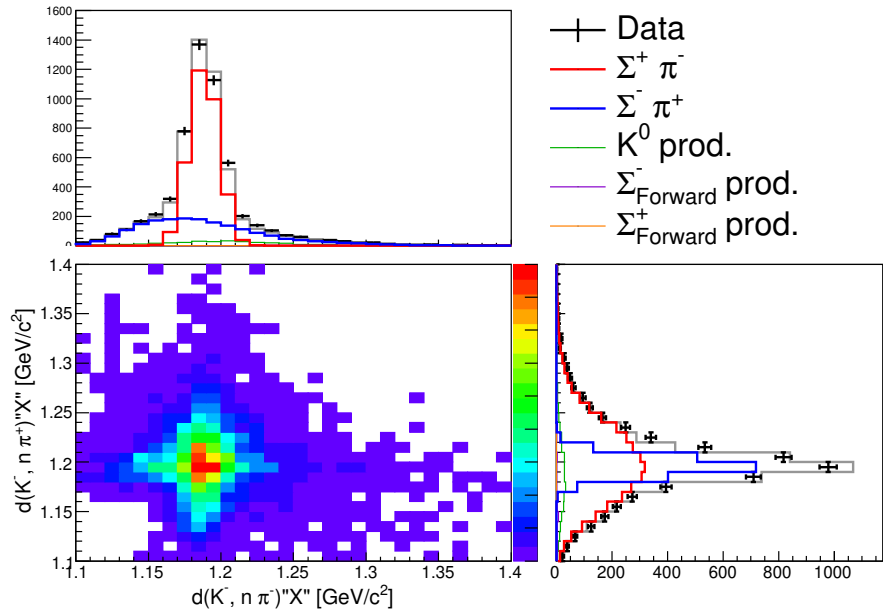


Figure 4.6: This figure shows template fitting of the  $d(K^-, n\pi)$  spectra to separate the  $\pi^- \Sigma^+$  and  $\pi^+ \Sigma^-$  modes. The down left figure shows two-dimensional plots of  $d(K^-, n\pi^-)$  and  $d(K^-, n\pi^+)$  on the horizontal and vertical axes, respectively. The top and right figures show the projection of each axis. The caption is same as Figure 4.5.

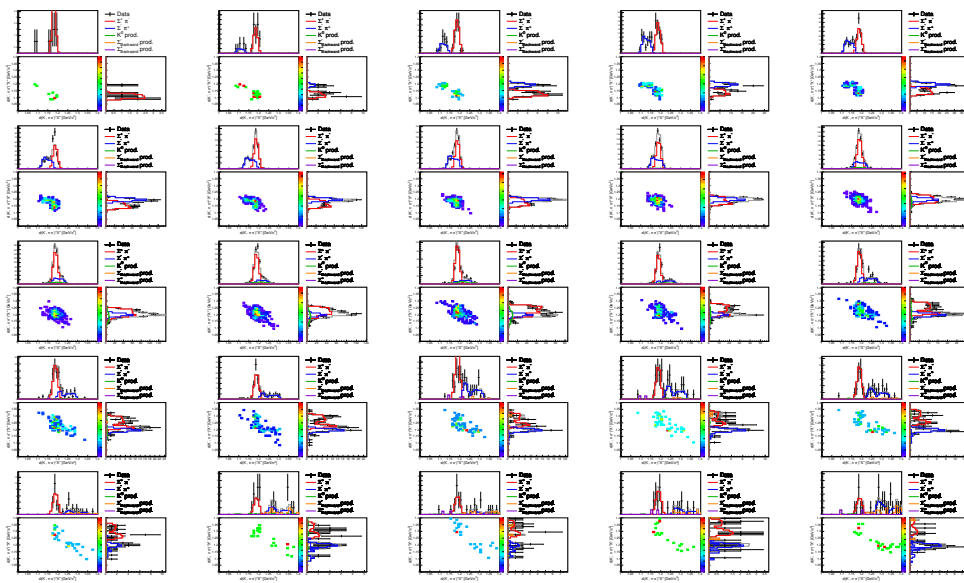


Figure 4.7: These figures are presented separately for each bin of  $d(K^-, n)$  for fitting to separate  $\pi^-\Sigma^+$  and  $\pi^+\Sigma^-$  modes. The top left figure shows the lowest missing mass in the 1.35-1.36GeV bin, with the next bin represented as one goes to the right. In other words, one row is shown for the 0.05GeV region.

$d(K^-, n\pi^+)$  from events that exclude background contributions from  $K^0$  and  $\Sigma_{forward}^\pm$  production in the  $K^-d \rightarrow n\pi^+\pi^-n$  final state as shown in Figure 4.6.

The lower left figure is a two-dimensional plot of  $d(K^-, n\pi^+)$  and  $d(K^-, n\pi^-)$ , while the upper and left figures display the one-dimensional spectra of the respective projections. These one-dimensional spectra were used for fitting. This figure represents the sum of the fitting results for all bins of  $d(K^-, n)\pi\Sigma$ , and the individual diagrams for each bin are presented in Figure 4.7. The notations in the figure are consistent with those used for background fitting (Figure 4.5). The background, represented by the green, purple, and orange lines, is removed within the  $3\sigma$  region, resulting in minimal leakage, though it is still accounted for. The signal, such as the red line indicating the  $\pi^-\Sigma^+$  mode, creates a peak in the  $d(K^-, n\pi^-)$  missing mass (top panel) consistent with the missing  $\Sigma$ , while the  $d(K^-, n\pi^+)$  missing mass (right panel) for the opposite charge do not form a peak but rather show a broad distribution. The opposite charge mode,  $\pi^+\Sigma^-$ , exhibits similar behavior when the charge is reversed. The values of  $-2\ln(\Lambda)/NDF \sim \chi^2/NDF$  for each bin of  $d(K^-, n)\pi\Sigma$  are shown in Figure 4.8. These fittings yield the  $\pi^-\Sigma^+$  and  $\pi^+\Sigma^-$  spectra shown in Figure 4.9, which are converted to a two-differential cross section by applying luminosity after acceptance correction, which is described in the next subsection.

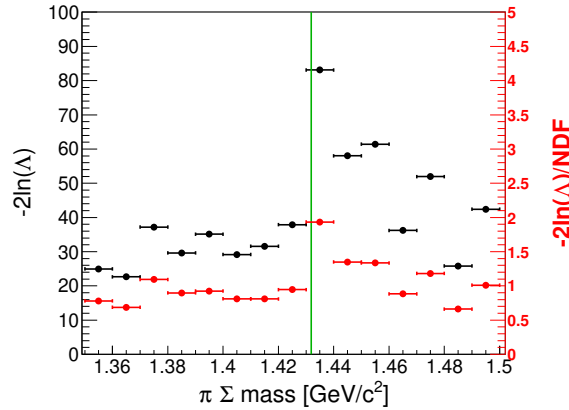


Figure 4.8: This figure shows the template fitting  $-2\log\Lambda$  and  $-2\log\Lambda/NDF$  for the separation of  $\pi^-\Sigma^+$  and  $\pi^+\Sigma^-$  modes in each  $d(K^-, n)$  bin. Black and red indicate  $-2\log\Lambda$  and  $-2\log\Lambda/NDF$ , respectively. The horizontal axis is represented for  $d(K^-, n)$  bins.

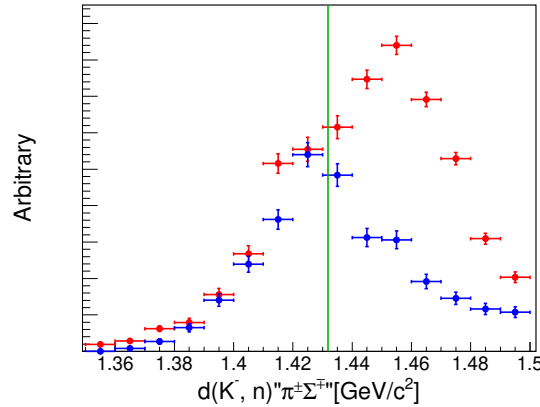


Figure 4.9: The  $\pi^-\Sigma^+$  and  $\pi^+\Sigma^+$  mode spectra with arbitrary scale by template fitting are shown. Red and blue lines indicate  $\pi^-\Sigma^+$  and  $\pi^+\Sigma^+$ , respectively. Green vertical line is indicated the  $\bar{K}N$  threshold.

## 4.2 Conversion to the cross section

The  $d(K^-, n)\pi^\pm\Sigma^\pm$  spectra obtained in the previous subsection and the  $d(K^-, p)\pi^-\Sigma^0$  spectrum obtained in Section ?? are scaled by the luminosity, the detection efficiency of detectors, and the solid angle of the forward detector. Their values are summarized in Table 4.1 for  $d(K^-, n)\pi^\pm\Sigma^\pm$  and in Table 4.2 for  $d(K^-, p)\pi^-\Sigma^0$ . In addition, the acceptance of the CDS, depending on the  $\pi\Sigma$  masses, is evaluated using Monte Carlo simulations generated according to a uniform  $\pi\Sigma$  mass distribution, where  $\pi^\pm\Sigma^\pm$  is as described in the previous section, and  $\pi^-\Sigma^0$  is generated in a similar way.

The luminosity consists of the thickness of the target and the number of beams irradiated. Target thickness is explained in Section ???. The number of irradiated beams is divided into the total number of Kaon beams irradiated, the fraction of these that actually pass through the fiducial volume of the target, the DAQ live ratio, which is the fraction that the DAQ accumulates as events that can be analyzed, and the trigger efficiency, which is the fraction of trigger signals produced. The fraction of beams that pass through the fiducial volume is explained in Section ???. The DAQ live ratio and the trigger efficiency are explained in Section ???. These values are evaluated for each run and summed up. The values in the table are representative, and the error represents the fluctuation between runs.

Next is the detection efficiency. In the case of forward neutrons,  $d(K^-, n)\pi^\pm\Sigma^\pm$ , the detection efficiencies of the NC for forward neutrons and the CDC for the

Table 4.1: Summary table of  $d(K^-, n)$  scaling parameters

Component	value	error	value	error
Luminosity (/ $\mu b$ )	5927	158		
Target Length (cm)			10	
Target density [ $g/cm^3$ ]			0.1613 – 0.1617	0.0015
Number of Kaon			$5.83 \times 10^{10}$	
Survival ratio of $K^-$			0.281	0.0003
DAQ live ratio			0.768	0.0021
Trigger efficiency				
$K \otimes CDH1$			0.9527	0.0004
Neutral			0.9992	$6.7 \times 10^{-6}$
Efficiency of the CDC	0.977	0.04		
Efficiency of the NC	0.291	0.015		
Intrinsic the NC			0.317	0.016
Over veto of the CVC/BVC			0.081	0.007
Solid angle of the NC (msr)	21.5	0.2		

Table 4.2: Summary table of  $d(K^-, p)$  scaling parameters

Component	value	error	value	error
Luminosity (/ $\mu b$ )	2478	81		
Target Length (cm)			10	
Target density [ $g/cm^3$ ]			0.1624	0.0014
Number of Kaon			$2.05 \times 10^{10}$	
Survival ratio of $K^-$			0.336	0.0001
DAQ live ratio			0.821	0.0001
Trigger efficiency				
$K \otimes CDH1$			0.9527	0.0003
Charge			0.9559	0.0004
Efficiency of the CDC	0.977	0.04		
Efficiency of the forward detectors	0.819	0.042		

two charged  $\pi$  are taken into account. The detection efficiency of the CDC is explained in Section ???. The detection efficiency of the NC is divided into the intrinsic detection efficiency of the NC, as discussed in Section ??, and the effect of overkill caused by the CVC and the PC installed to veto charged particles, which is explained in Section ???. In the case of forward protons,  $d(K^-, p)\pi^-\Sigma^0$ , the charged  $\pi$  were also detected using the CDC, while the FDC1 and the PC/CVC were used for detecting forward protons. The detection efficiencies for these detectors are described in Section ??.

Next is the solid angle of the forward detector. In the case of forward neutrons, since the neutron flight path is a straight line, it can be simply calculated from the position of the NC. The solid angle is estimated from the center position of the NC, and its error is determined by the thickness of the NC. On the other hand, for forward protons, the calculation is not straightforward due to the momentum dependence caused by bending from the Beam Sweeping Magnet, so we used Monte Carlo simulation to evaluate the solid angle. In that simulation, the effect of multiple scattering was estimated, and other reactions, such as elastic scattering, inelastic scattering, and hadron reactions, were cut off. Using that simulation, the forward protons passing through all six planes of FDC1 and the PC/CVC were treated as effective events. The effective rate was calculated for each infinitesimal piece of solid angle, weighted accordingly, and then summed together to obtain the total solid angle. The relationship between the  $\pi^-\Sigma^0$  mass and solid angle obtained by this method is shown in Figure 4.10.

In the CDS acceptance correction, the trigger event is defined on the condition that a forward-irradiated neutron or proton passes through the corresponding forward detector and can be analyzed. For example, in the case of forward neutrons, the trigger event is defined by an event in which a forward-irradiated neutron passes through the NC and produces an energy deposit above 8 MeVee in the NC. An acceptable event is defined as one where the same analysis procedure is applied to the real data and the event remains until the final selection. For example, in the case of  $d(K^-, n)\pi^\mp\Sigma^\pm$ , an acceptable event is one where  $\pi^+$  and  $\pi^-$  are detected individually in the CDS, and the missing neutron can be identified from the  $d(K^-, n\pi^+\pi^-)$  missing mass, while background contributions from  $K^0$  and  $\Sigma_{forward}^{pm}$  are removed. In the case of  $d(K^-, p)\pi^-\Sigma^0$ , an acceptable event is one in which two  $\pi^-$  are detected in the CDS,  $\Sigma^0$  is identified from the missing mass of  $d(K^-, p\pi^-)$ , and the  $p\gamma$  is determined from the missing mass of  $d(K^-, p\pi^-\pi^-)$ . The CDS acceptances for  $d(K^-, n)\pi^\mp\Sigma^\pm$  and  $d(K^-, p)\pi^-\Sigma^0$ , obtained using these methods, are shown in Figures 4.11 and 4.12, respectively. By applying

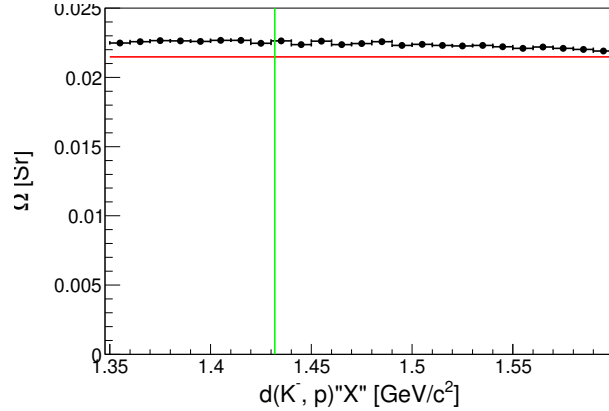


Figure 4.10: This figure shows the relationship between the mass of  $\pi^-\Sigma^0$  and the solid angles of the forward detector, FDC1 and PC/CVC with respect to the irradiated forward proton. The red line represents the solid angle of the NC detector with respect to the forward neutron.

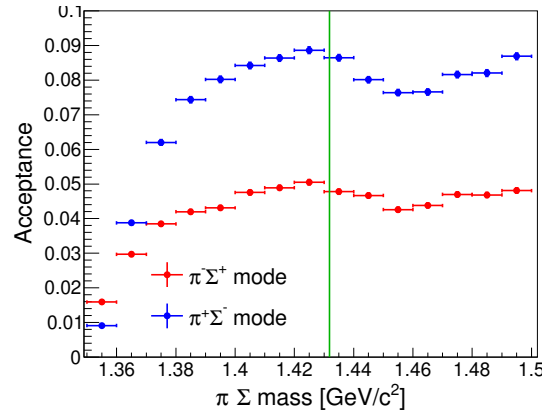


Figure 4.11: This figure shows the acceptance of  $d(K^-, n)\pi^\pm\Sigma^\pm$ . The red line indicates  $\pi^-\Sigma^+$  and the blue line indicates  $\pi^+\Sigma^-$ .

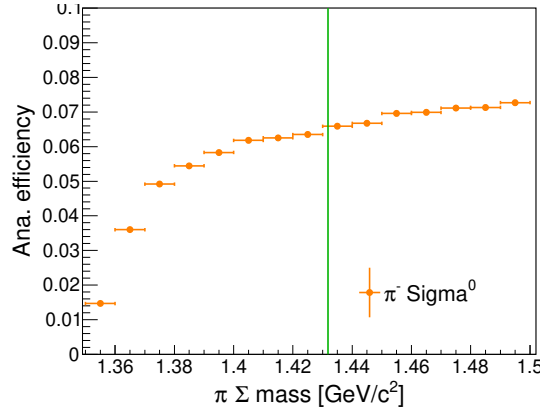


Figure 4.12: This figure shows  $d(K^-, p)''\pi^-\Sigma^0''$  acceptance

the CDS acceptance correction, the double differential cross sections for  $d(K^-, n)\pi^\mp\Sigma^\pm$  and  $d(K^-, p)\pi^-\Sigma^0$  are obtained, as shown in Figures 4.13 and 4.14. The thin boxes indicate statistical errors, the thick boxes include fitting errors, and the error bars represent the total errors, including those from conversion coefficients.

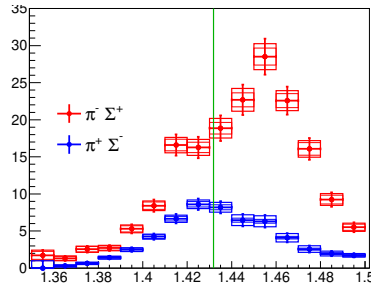


Figure 4.13: The red figure and blue figure shows about  $d(K^-, n)''\pi^+\Sigma^-''$  and  $d(K^-, n)''\pi^-\Sigma^+''$ , respectively. The inner frame (thin line), outer frame (thick line), and error bars represent the addition of statistical errors, fitting errors, and conversion errors, which were calculated by root-mean-square. The green vertical lines indicates  $\bar{K}N$  threshold.

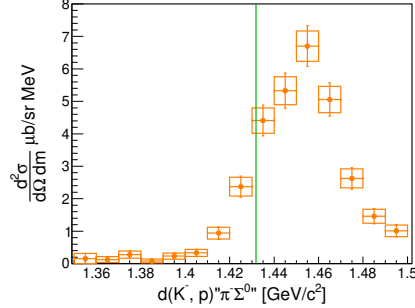


Figure 4.14: This figure shows the cross section of  $d(K^-, p)''\pi^-\Sigma^0''$ . The box represents the statistical error, and the error bar represents the root mean squares of the conversion factor added to it. The green vertical lines indicates  $\bar{K}N$  threshold.

### 4.3 Spectra

#### 4.3.1 Qualitative properties of obtained spectra

In this subsection, we discuss the physical meaning of the obtained spectra. The  $d(K^-, n)\pi^\mp\Sigma^\pm$  and  $d(K^-, p)\pi^-\Sigma^0$  spectra, which were obtained in the previous section, are considered. Additionally, the  $d(K^-, n)K^0n$  spectra, discussed in Appendix ??, are also included. That spectra do not provide information below the  $\bar{K}N$  threshold but offer a good indication for examining  $K^-N \rightarrow \bar{K}N$  scattering. It is noted that approximately 14% of the spectra contain contributions from possible two-step reactions, as explained in Appendix ???. This value is consistent at the order level with the  $d(K^-, N)\pi\Sigma$  spectra, suggesting that it is reasonable to assume this spectrum is a 2-step reaction. The bump structure in the  $d(K^-, n)K^0n$  spectrum rising from the  $\bar{K}N$  threshold is due to a reaction so-called quasi-elastic scattering, where the  $K^-$  kicks out the neutron, resulting in this form without the involvement of other nucleons in the reaction. The spectrum of  $d(K^-, p)\pi^-\Sigma^0$  is similar to this quasi-elastic scattering because the  $\bar{K}N \rightarrow \pi^-\Sigma^0$  scattering has isospin  $I = 1$  and lacks a pole near the threshold. In contrast, The  $d(K^-, n)\pi^-\Sigma^+$  spectrum exhibits an excess structure below the  $\bar{K}N$  threshold in addition to the quasi-elastic scattering, possibly due to the  $I = 0$  pole of the  $\bar{K}N \rightarrow \pi\Sigma$  scattering occurring below threshold. On the other hand, the shape of the  $d(K^-, n)\pi^+\Sigma^-$  spectrum is significantly different from that of the  $d(K^-, n)\pi^-\Sigma^+$  spectrum, with these differences attributed to interference terms at isospin  $I = 0$  and  $I = 1$ .

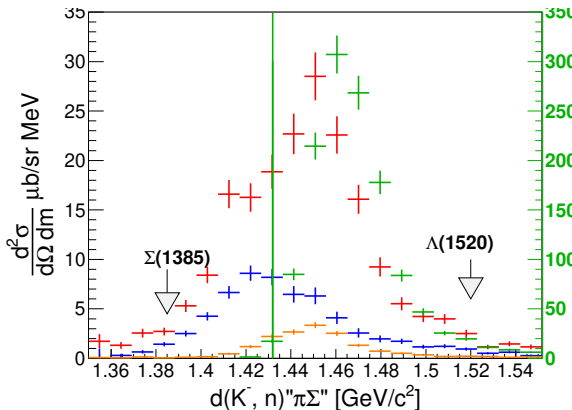


Figure 4.15: The obtained cross sections are plotted simultaneously in this figure. The  $d(K^-, n)\pi^-\Sigma^+$ ,  $d(K^-, n)\pi^+\Sigma^-$ ,  $d(K^-, n)nK^0$ , and  $d(K^-, p)\pi^-\Sigma^0$  plot as red, blue, green, and orange, lines respectively. The  $d(K^-, n)nK^0$  is scaled to 1/10. The green vertical line indicates the  $\bar{K}N$  threshold.

Around the  $\bar{K}N$  threshold, there are known to be the  $\Sigma(1385)$ , which is a  $P$ -wave with  $I = 1$ , and the  $\Lambda(1520)$ , which is a  $D$ -wave with  $I = 0$ . There is no structure around  $\Sigma(1385)$  in our  $d(K^-, p)\pi - \Sigma^0$  spectrum with  $I = 1$ , nor around  $\Sigma(1385)$  or  $\Lambda(1520)$  in the  $d(K^-, n)\pi^\mp\Sigma^\pm$  spectrum, which has contributions from both  $I = 0$  and  $I = 1$ . This indicates that the obtained spectra are dominated by S waves, and higher-order contributions from  $P$ -waves,  $D$ -waves, and other states have little effect on the results.

Summarizing, the obtained spectra indicate that the second-step  $\bar{K} \rightarrow \pi\Sigma$  scattering is dominated by S-waves. The  $d(K^-, n)\pi^\mp\Sigma^\pm$  spectrum with  $I = 0$  exhibits a structure below the  $\bar{K}N$  threshold, and the difference between the two spectra also suggests an interference term between  $I = 0$  and  $I = 1$ .

### 4.3.2 Comparison with theoretical calculations

In the previous section, we discussed the qualitative properties of the spectrum; in this section, we will examine our spectrum in more detail by comparing it with the kinematics-based theoretical calculations for this experiment. These calculations assume that the reaction is a 2-step reaction described in Chapter 1, which, as discussed in the previous section, is reasonable based on the  $d(K^-, n)K^0n$  spectrum.

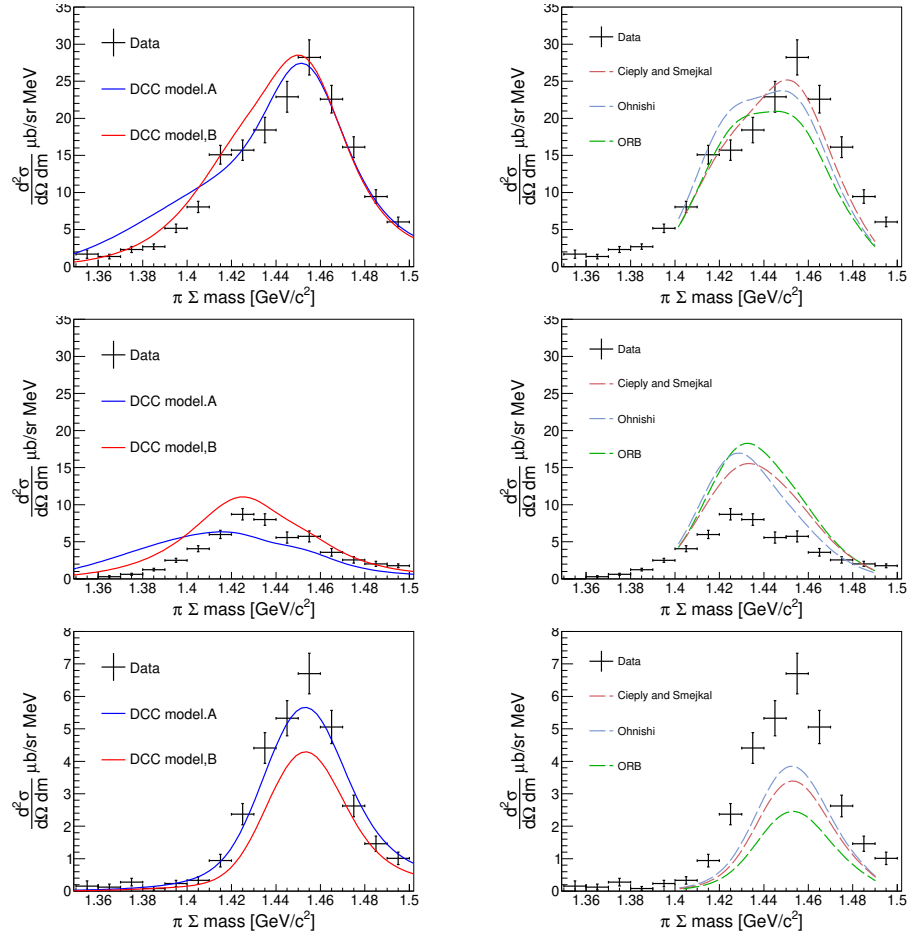


Figure 4.16: This figure shows a comparison of our obtained spectra with predictions from theoretical calculations. The top, middle, and bottom figures represent  $\pi^-\Sigma^+$ ,  $\pi^+\Sigma^-$ , and  $\pi^-\Sigma^0$ , respectively. The right figure shows the spectrum predicted by the DCC model [42], and the left figure shows the spectrum predicted by the calculation of Miyagawa et al [38]. The spectra predicted by theoretical calculations are convoluted with our detector resolution.

Theoretical calculations of this experiment have been published by Miyagawa et al. [38] and by Kamano et al. using the Dynamical Coupled Channel (DCC) method [42]. The method of Miyagawa et al. employs the results of partial wave analysis for the first step  $K^-N \rightarrow \bar{K}N$  scattering and the results of various chiral analyses for the second step  $\bar{K}N \rightarrow \pi\Sigma$  scattering, i.e., these two scattering amplitudes are not continuously connected.

On the other hand, the DCC method fits almost all available  $K^-p \rightarrow$  meson-baryon scattering data over a wide mass range to obtain the scattering amplitudes, and the scattering amplitudes of the first and second steps can be connected continuously. The  $\bar{K}N \rightarrow \pi\Sigma$  scattering amplitude used by Miyagawa et al. includes three variations: a historical analysis by E. Oset, A. Ramos, and C. Bennhold [39]; an analysis by Ohnishi et al. using the AGS equation [41]; and an analysis by A. Cieplý and J. Smejkal utilizing SHIDDARTA data [40]. The two sets of parameters, known as Model A and Model B, are provided by the DCC method. The pole parameters of the  $\Lambda(1405)$ , which has  $I = 0$  and is located below the  $\bar{K}N$  threshold, differ significantly due to the lack of low-momentum data. Figure ?? shows our data alongside the theoretical calculations. The spectra of  $\pi^-\Sigma^+$ ,  $\pi^+\Sigma^-$ , and  $\pi^-\Sigma^0$  are presented from the top panel downwards. The left panels display the results obtained using the DCC method, while the right panels show the calculations by Miyagawa et al..

The spectral shapes of all theoretical calculations appear to reproduce the characteristics of all pi Sigma modes in the data we observed. However, while the DCC method explains the strength for all  $\pi\Sigma$  modes, the Miyagawa et al. calculations are in good agreement for  $\pi^-\Sigma^+$ , but greatly exceed the values of our observed data for  $\pi^+\Sigma^-$  and fall far short for  $\pi^-\Sigma^0$ . The  $\pi^-\Sigma^0$  spectrum has  $I = 0$ , while the  $\pi^\mp\Sigma^\pm$  spectrum exhibits both  $I = 0$  and  $I = 1$  effects. Changes in one affect the other, making it challenging to achieve a comprehensive fit in Miyagawa's calculations. This suggests the importance of establishing a continuous connection between the responses of the first step and the second step, i.e., a consistent scattering amplitude in widely region.

#### 4.3.3 $\bar{K}N$ Pole parameters assuming the 2-step reaction

Next, we discuss the method for obtaining the  $\bar{K}N$  pole parameters through fitting under the assumption of a 2-step reaction. This approach is similar to that used by Noumi et el., as introduced in Chapter 1. Since this analysis method focuses only on  $I = 0$ , the obtained spectra are separated into components of  $I = 0$ . In this procedure, the spectra are further separated

into components of  $I = 1$  and, in addition, the interference term between  $I = 0$  and  $I = 1$ . The obtained spectrum can be expressed as follows from the isospin relation.

$$\begin{aligned} \frac{d\sigma}{d\Omega dM}(\pi^\mp\Sigma^\pm) &\propto |C_{K^-N\rightarrow\bar{K}N}^0 T_{\bar{K}N\rightarrow\pi\Sigma}^{I=0} \mp C_{K^-N\rightarrow\bar{K}N}^1 T_{\bar{K}N\rightarrow\pi\Sigma}^{I=1}|^2 \\ &= |C_{K^-N\rightarrow\bar{K}N}^0 T_{\bar{K}N\rightarrow\pi\Sigma}^{I=0}|^2 + |C_{K^-N\rightarrow\bar{K}N}^1 T_{\bar{K}N\rightarrow\pi\Sigma}^{I=1}|^2 \\ &\mp 2\text{Re}(C_{K^-N\rightarrow\bar{K}N}^0 C_{K^-N\rightarrow\bar{K}N}^1 T_{\bar{K}N\rightarrow\pi\Sigma}^{I=0} T_{\bar{K}N\rightarrow\pi\Sigma}^{I=1}) \end{aligned} \quad (4.1)$$

$$\frac{d\sigma}{d\Omega dM}(\pi^-\Sigma^0) \propto |C_{K^-N\rightarrow\bar{K}N}^1 T_{\bar{K}N\rightarrow\pi\Sigma}^{I=1}|^2 \quad (4.2)$$

Here,  $T_{\bar{K}N\rightarrow\pi\Sigma}^{I=0,1}$  represents the  $T$  matrix of the second  $\bar{K}N \rightarrow \pi\Sigma$  scattering for isospin  $I = 0$  and  $I = 1$ . Additionally,  $C_{K^-N\rightarrow\bar{K}N}^{0,1}$  denotes the factor for the first  $K^-p \rightarrow \bar{K}N$  scattering, corresponding to the isospin  $I = 0$  and  $I = 1$  components of the second scattering.

Since it can be expressed as shown in Equation (4.1), (4.2), the spectra corresponding to  $I = 0$ ,  $I = 1$ , and their interference terms can be written as follows.

$$\frac{d\sigma}{d\Omega dM}(I = 0) \propto \frac{1}{2} \left( \frac{d\sigma}{d\Omega dM}(\pi^-\Sigma^+) + \frac{d\sigma}{d\Omega dM}(\pi^+\Sigma^-) - \frac{d\sigma}{d\Omega dM}(\pi^-\Sigma^0) \right) \quad (4.3)$$

$$\frac{d\sigma}{d\Omega dM}(I = 1) \propto \frac{d\sigma}{d\Omega dM}(\pi^-\Sigma^0) \quad (4.4)$$

$$\frac{d\sigma}{d\Omega dM}(\text{int}) \propto \left( \frac{d\sigma}{d\Omega dM}(\pi^-\Sigma^+) - \frac{d\sigma}{d\Omega dM}(\pi^+\Sigma^+) \right) \quad (4.5)$$

The 2-step response can be expressed as follows,

$$\frac{d\sigma}{dM_{\pi\Sigma} d\Omega_n} = \left| \langle n_{\theta=0} \pi\Sigma | T_{\bar{K}N_2\rightarrow\pi\Sigma}^2 G_0(\bar{K}, N_2) T_{K^-N_1\rightarrow\bar{K}N}^1 | K^- \Phi_d \rangle \right|^2$$

where  $G_0(\bar{K}, N_2)$ , represents the Green's function describing the propagation of virtual  $\bar{K}$  mesons between the first and second scattering steps. This equation can be factorized using the deuterium wavefunction  $\psi_d(p)$  and decomposed into a 1-step response  $f_{res}(M_{\pi\Sigma})$  function and a 2-step scattering amplitude as shown below.

$$\begin{aligned} \frac{d\sigma}{dM_{\pi\Sigma} d\Omega_n} &\sim \left| T_{\bar{K}N_2\rightarrow\pi\Sigma}^2 \right|^2 F_{res}(M_{\pi\Sigma}) \\ F_{res}(M_{\pi\Sigma}) &= \left| \int G_0(\bar{K}, N_2) T_{K^-N_1\rightarrow\bar{K}N}^1 \psi_d(p) d^3 p_N \right|^2 \end{aligned}$$

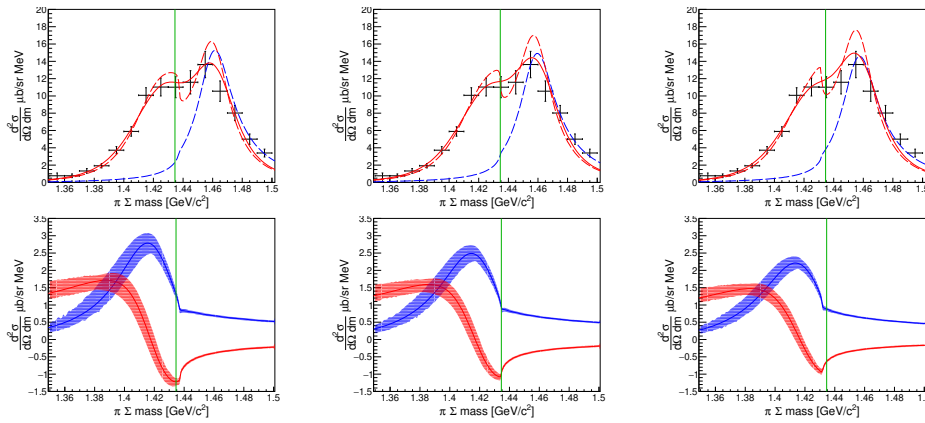


Figure 4.17: This figure shows the  $I = 0$  spectrum obtained from Eq. (4.3) and the fit results assuming a 2-step reaction. In the upper panel, the error bars represent the experimental data, the red line indicates the spectrum resulting from the fit, the solid line corresponds to the spectrum convolved with detector resolution, and the dashed line represents the spectrum without resolution. The lower panel displays the scattering amplitude for the two-step  $\bar{K}N \rightarrow \bar{K}N$  scattering, where the red line indicates the real part and the blue line shows the imaginary part. The lines are the best-fit values and the bands hatched in color represent the width of the error due to fitting.

The  $T$ -matrix of the second scattering is expressed as follows, utilizing the low-energy expansion up to the second order for the two channels [63].

$$T_{\bar{K}N \rightarrow \bar{K}N}^2 = \frac{A}{1 - iAk_2 + \frac{1}{2}ARk_2^2}$$

$$T_{\bar{K}N \rightarrow \pi\Sigma}^2 = \frac{e^{i\delta}}{\sqrt{k_1}} \frac{\sqrt{\text{Im}A - \frac{1}{2}|A|^2\text{Im}Rk_2^2}}{1 - iAk_2 + \frac{1}{2}ARk_2^2}$$

This fit includes the scattering length  $A$  and the effective range  $R$  of the second-step scattering, along with a parameter determining the overall scale. In other words, the shape of the first-step scattering (reaction function) is fixed, and the spectrum shape is determined solely by the second-step scattering. The scattering length and effective range are complex numbers, so there are five free parameters in total. This fitting is performed using three  $\bar{K}N$  threshold values:  $K^-p$ ,  $\bar{K}N$  (the average of  $K^-p$  and  $K^0n$ ), and  $K^0n$ . The discrepancies in the results arising from the differences in threshold values are evaluated as a source of systematic error. These differences in threshold values are reflected not only in the mass of the  $\bar{K}N$  channel in the  $T$ -matrix of the second-scattering but also in the mass of the nucleon used to calculate the response function in the first-step scattering. The figure above shows the results of the fit: black error bars represent the data, and the red solid line shows the fit results convolved with detector resolution, which are used to calculate the chi-square. The red dashed line shows the fit spectrum without detector resolution, and the blue dashed line indicates the response function, scaled arbitrarily. The figure below shows the scattering amplitude obtained from the fit, with red and blue representing the real and imaginary parts, respectively. The lines indicate the best-fit result, and the bands show the error range, determined by the maximum and minimum values when adjusting the real and imaginary parts of  $A$  and  $R$  within their error margins. The central values of the parameters and the fitting errors were evaluated in terms of the average  $\bar{K}N$  threshold, with  $A = -1.05 \pm 0.12(\text{fit.}) \pm +0.09(\text{syst.}) + [0.86 \pm 0.15(\text{fit.})]_{-0.08}^{+0.07}(\text{syst.})i$  and  $R = -0.22 \pm 0.40(\text{fit.})]_{-0.06}^{+0.05}(\text{syst.}) + [-0.42 \pm 0.16(\text{fit.})]_{-0.08}^{+0.12}(\text{syst.})i$ . These values need to be converted to the pole's position [MeV] and width [MeV], where the pole is defined by setting the denominator of the  $T$ -matrix to zero, i.e., by solving the following equation.

$$\frac{1}{2}ARk^2 + Ak^2 + 1 = 0 \quad (4.6)$$

Where  $k$  is the momentum of the  $\bar{K}N$  center-of-mass system, converted to

mass by  $m = \sqrt{m_{KN}^2 + k^2}$ .

Since  $A$  and  $R$  are complex numbers, propagating their errors is not straightforward. Therefore, the position and width errors of the poles are estimated by generating a Gaussian distribution using the real and imaginary parts of  $A$  and  $R$  as random variables, with fitting errors as the standard deviation  $\sigma$ . This approach is similar to the conventional error propagation method, which treats each parameter as an independent Gaussian, with the overall error as a composite of Gaussian distributions. Figure 4.18, 4.19 shows the resulting distribution of position and width. These distributions are clearly asymmetric, particularly in terms of width, due to a threshold effect caused by the proximity of the thresholds.

$$f_{fit}(x) = \begin{cases} A \exp\left(-\frac{(x-M)^2}{2\sigma_h^2}\right) & (x > M) \\ A \exp\left(-\frac{(x-M)^2}{2\sigma_l^2}\right) & (x < M) \end{cases}$$

Here,  $M$  represents the central value, with  $\sigma_h$  and  $\sigma_l$  denoting the errors in the high and low regions, respectively. This function explicitly distinguishes between errors above and below the central value while ensuring continuity at  $M$ . The distribution includes a tail component that deviates from a Gaussian profile, which must be excluded for accurate error evaluation. To achieve this, the evaluation range is divided into several regions, each corresponding to a percentage of the peak height, and the fit is performed in each region. For instance,  $\exp(-\frac{1}{2}3^2)$  corresponds to the  $\pm 3\sigma$  region. This fitting process was conducted for all regions, ranging from  $3\sigma$  to  $1\sigma$ , with increments of  $0.5\sigma$ . Figure 4.20 shows the relationship between the reduced  $\chi^2/NDF$  and the cut range for each fit. Here, the  $\chi^2/NDF$  increases from the entire region to  $3\sigma$ . This is thought to be due to the limited improvement in the fit because the tail component was not fully removed, as well as the decrease in  $NDF$  resulting from the narrower range. The  $\chi^2/NDF$  seems to reach saturation at the  $1.5\sigma$  range. Therefore, a range of  $1.5\sigma$  is chosen as a reference to determine the position and width of the pole of  $\Lambda(1405)$ , which is found to be  $1418.3^{+7.5}_{-2.4}(fit.)^{+0.9}_{-1.1}(syst.) + [-27.8^{+9.5}_{-0.9}(fit.)^{+1.9}_{-2.1}(syst.)]i$  [MeV]. Here, the central value is determined from the scattering length and the effective range of the best fit. The fitting errors are evaluated using the average of  $K^0 n$  and  $K^- p$  for the threshold values, and the systematic errors were assessed by varying the threshold values.

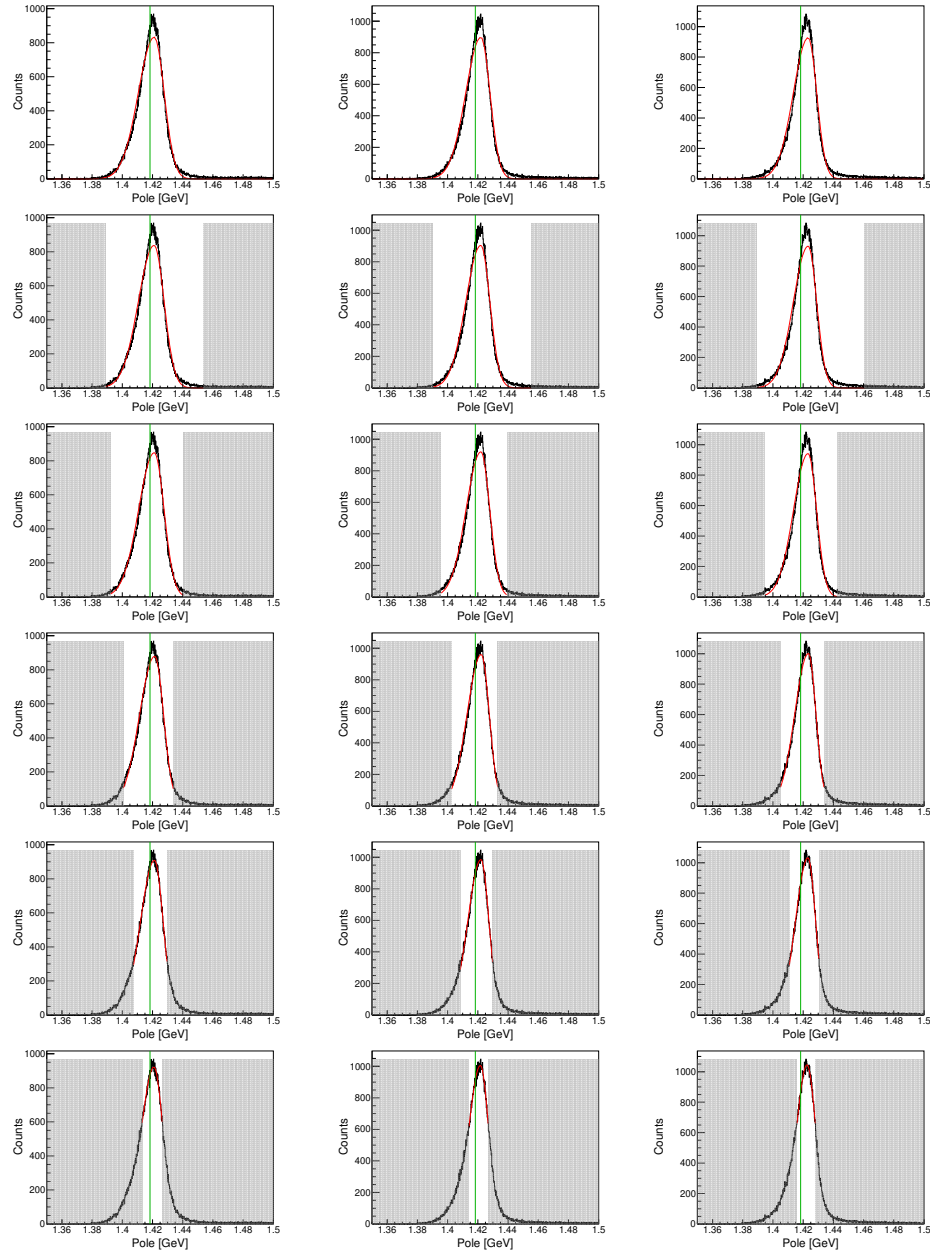


Figure 4.18: This figure shows the distribution and fit of the poles of  $\Lambda(1405)$ , generated using Gaussian random numbers. The right, center, and left panels correspond to the results based on the  $K^-p$ ,  $\bar{K}N$ , and  $K^0n$  thresholds, respectively. The top row represents the fit over the entire range, followed by rows corresponding to the equivalent ranges of  $3\sigma$ ,  $2.5\sigma$ ,  $2\sigma$ ,  $1.5\sigma$ , and  $1\sigma$ . The fit results are shown as red lines, with gray hatched areas representing regions excluded from the fit. The green lines indicate the pole positions corresponding to the best-fit values shown in Figure 4.17.

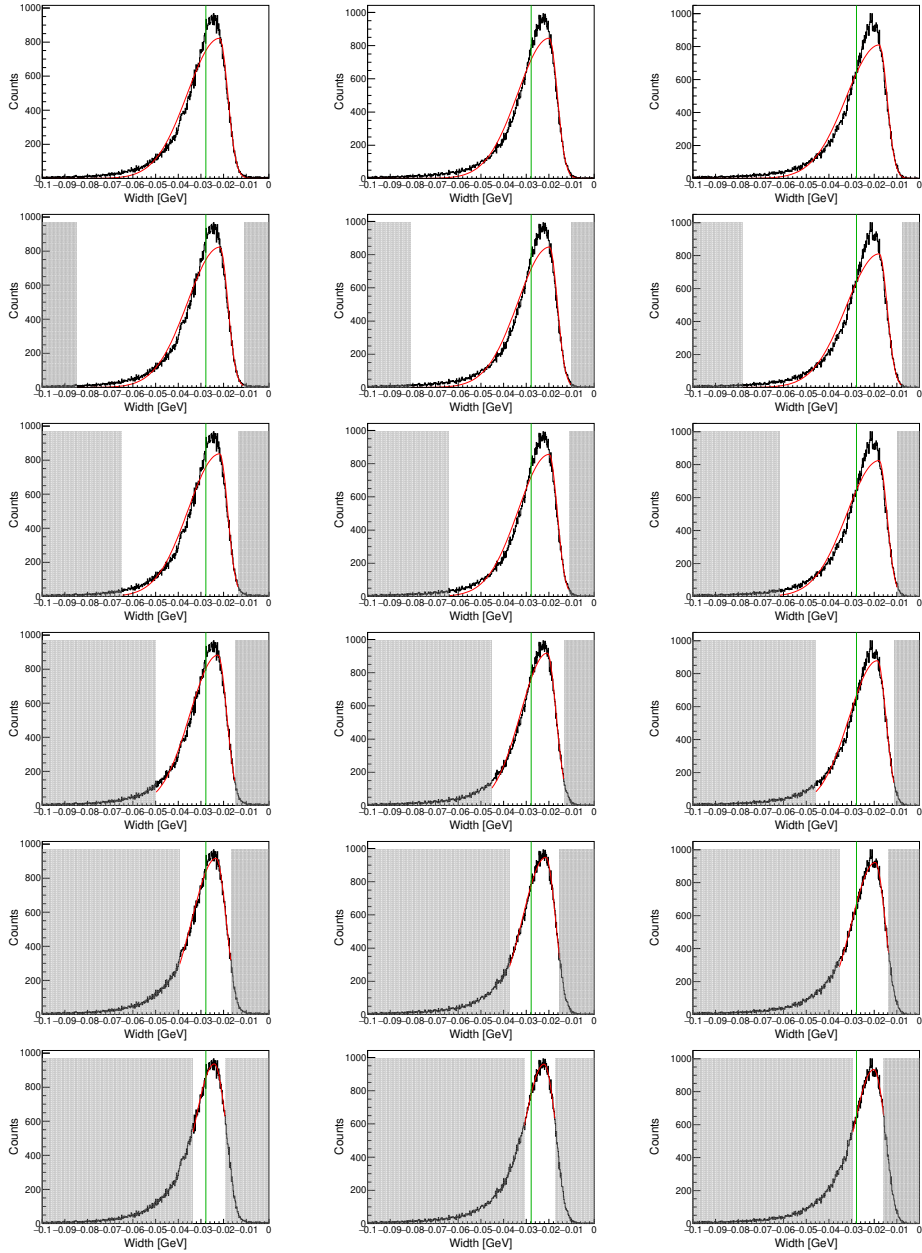


Figure 4.19: This figure shows the distribution and fit of the widths of  $\Lambda(1405)$ , generated using Gaussian random numbers. The details of the figure caption are identical to those of Figure 4.18, which provides further context.

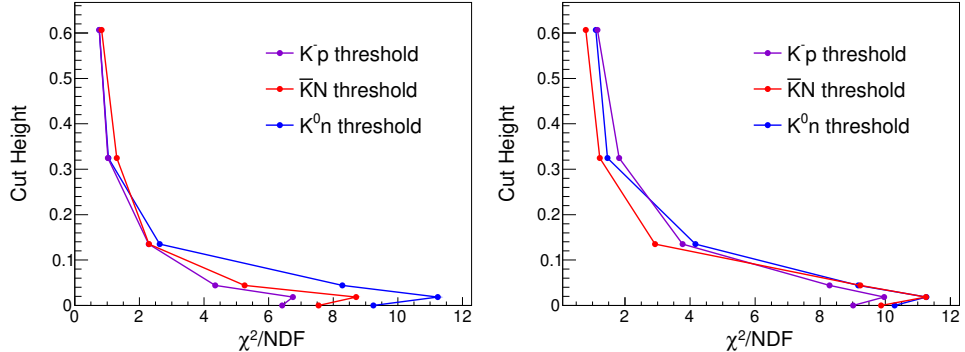


Figure 4.20: This figure illustrates the  $\chi^2/NDF$  relationship for the fittings of the  $\Lambda(1405)$  pole and width, as shown in Figures 4.18 and 4.19. The left panel corresponds to the pole fittings, while the right panel represents the width fittings. The purple, red, and blue lines indicate the results for the  $K^-p$ ,  $\bar{K}N$ , and  $K^0n$  thresholds, respectively.

#### 4.3.4 Comparison with DCC model

The method described in the previous section focused solely on the  $I = 0$  component, leaving  $I = 1$  and the interplay between  $I = 0$  and  $I = 1$  in the obtained spectra unexplored. To address this limitation, we will utilize spectra derived from the DCC model to examine these contributions. First, we fit the experimental spectra we obtained by introducing the parameters  $S_{I=0}$  and  $S_{I=1}$ , which adjust the strengths of  $I = 0$  and  $I = 1$  components independently. Two versions of the DCC model, Model A and Model B, are considered. Figures 4.21 and 4.22 correspond to cases using Model A and Model B, respectively. For the fitting performed with Model A, the parameter for  $I = 0$  was reduced to  $S_{I=0} = 0.562 \pm 0.015$ , while the parameter for  $I = 1$  remained nearly unchanged at  $S_{I=1} = 1.070 \pm 0.040$ . With Model B, the parameter for  $I = 0$  was reduced to  $S_{I=0} = 0.721 \pm 0.016$ , whereas the parameter for  $I = 1$  was increased to  $S_{I=1} = 1.423 \pm 0.055$ . Considering each figure, the  $I = 1$  spectrum appears to be in good agreement with both Models A and B. On the other hand, the spectra for the interference term and  $I = 0$  seem to align reasonably well with Model B, but not with Model A. In Model A, the fit for the interference term appears to lack intensity above the threshold, and the overall spectrum does not seem to match  $I = 0$ . In fact, the fitting with Model B yields  $\chi^2/NDF = 220/42 = 5.25$ , whereas the fitting with Model A is significantly worse, with  $\chi^2/NDF = 691/42 = 16.4$ . Table 4.3 lists the pole parameters of  $\Lambda(1405)$  derived from the DCC model,

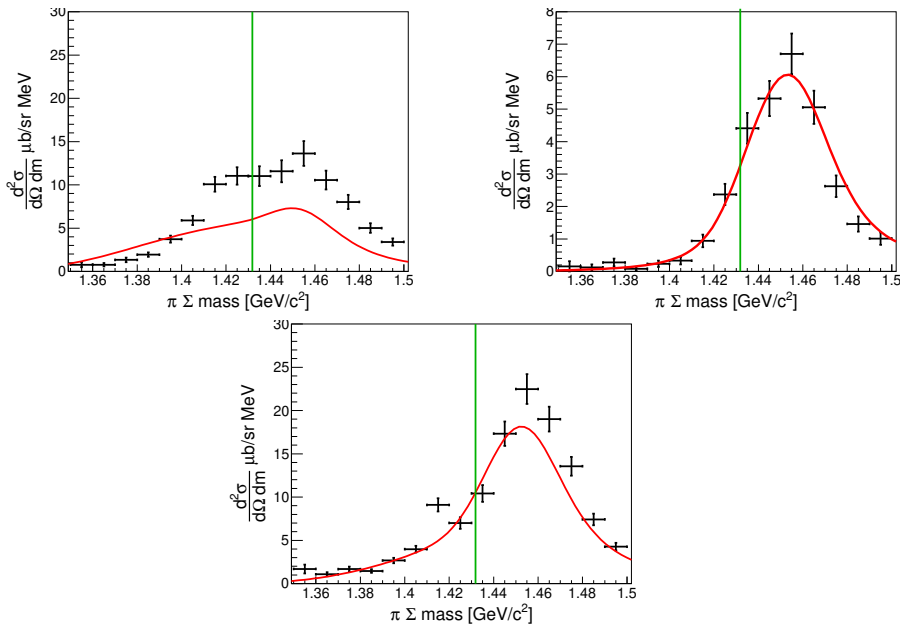


Figure 4.21: This figure illustrates the spectra of the experimental data, decomposed into  $I = 0$ ,  $I = 1$ , their interference terms, and the corresponding fitting results obtained using Model A of the DCC model. The black error bars represent the experimental data, while the red line denotes the fit results. The upper-left panel corresponds to  $I = 0$ , the upper-right panel to  $I = 1$ , and the lower panel to the interference term.

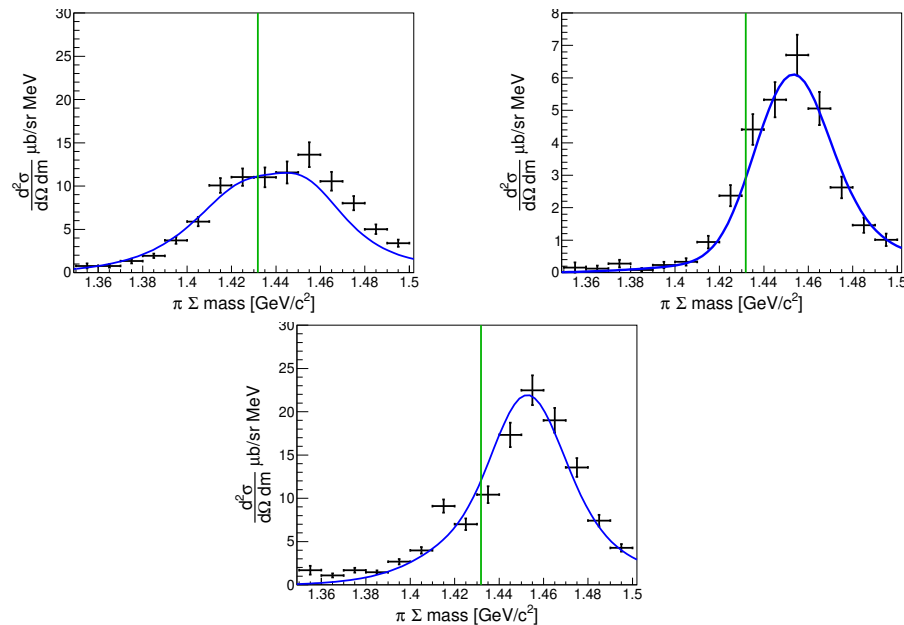


Figure 4.22: This figure presents the results of fitting the experimental data using Model B. The blue line represents the fit results, while other notations follow the same conventions as in Figure 4.21.

where Pole1, the higher of the two poles, significantly affects the observed spectrum. In model A, the imaginary part, or width, of that parameter is large, resulting in a pronounced tail of the  $I = 0$  spectrum below the  $\bar{K}N$  threshold, thus preventing accurate reproduction of the observed spectrum.

Table 4.3: This table shows the pole position with  $I = 0$  and  $J^P = 1/2^-$  below the  $\bar{K}N$  threshold by DCC models [42]

	pole1	pole2
Model.A	$1437 - 75i$	$1372 - 56i$
Model.B	$1428 - 31i$	$1397 - 98i$

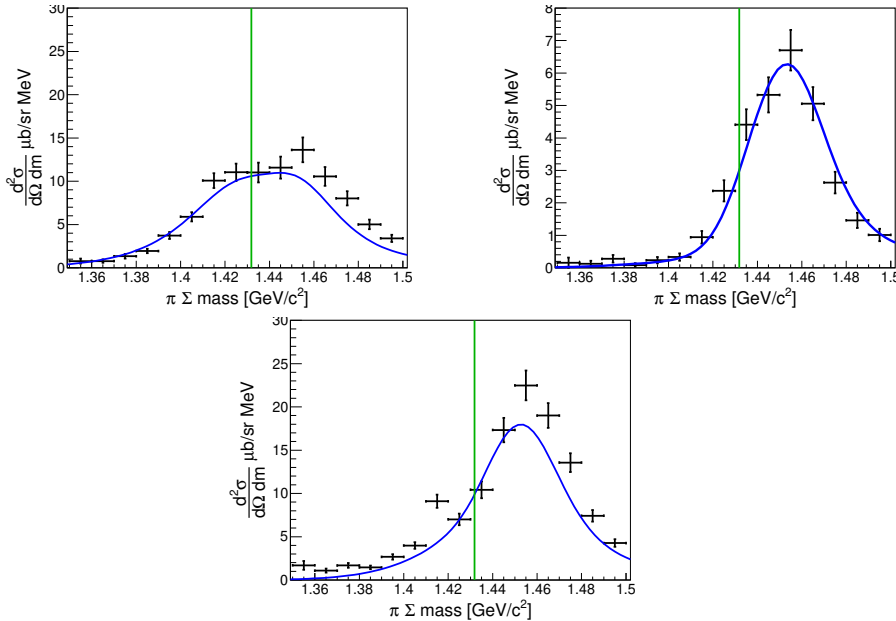


Figure 4.23: This figure shows the results of the fitting using Model.B with the introduction of parameters related to the interference term. The notation is the same as in Fig.4.22. In this fitting, the  $I = 1$  strength is determined only from the  $\pi^- \Sigma^0$  spectrum, while the other two parameters are determined from the  $\pi^- \Sigma^+$  and  $\pi^+ \Sigma^-$  spectra.

In more detail, the fitting in model B reveals that both the  $I = 0$  and  $I = 1$  spectra seem to lack intensity compared to the theoretical spectrum above the  $\bar{K}N$  threshold, while the interference term spectrum shows a

better fit. This means that the  $I = 0$  spectrum is determined below the  $\bar{K}N$  threshold, while above the  $\bar{K}N$  threshold, it is limited by the interference between  $I = 0$  and  $I = 1$ . In general, the scattering amplitude is complex, and there is flexibility to adjust its phase, i.e., to introduce a parameter representing the phase difference between  $I = 0$  and  $I = 1$ . If the phase difference is denoted by  $\theta_{I=0,1}$ , the relationship between the scale parameter, which modifies the magnitude of the interference term, and  $S_{int} = \cos \theta_{I=0,1}$  can be derived from the third term in Eq.4.1.

We fit the observed spectrum with DCC's Model B by introducing a free parameter that adjusts this interference term independently. The  $I = 1$  spectrum is determined only from the  $\pi^- \Sigma^0$  spectrum, whereas the  $I = 0$  spectrum is derived from all three  $\pi\Sigma$  spectra. The interference term is determined from the  $\pi^- \Sigma^+$  and  $\pi^- \Sigma^-$  spectra. Therefore, we first fit only the  $I = 1$  spectrum, fixed  $S_{I=1}$  at that value, and then performed a fit to determine both  $S_{I=0}$  and  $S_{int}$ , as shown in Figure 4.23. The  $\chi^2/NDF = 187/41 = 4.56$  of this fit is, which was improved by introducing a phase parameter. In this fit, the  $I = 0$  scale parameter  $A_{I=0}$  decreases from  $0.721 \pm 0.016$  to  $0.686 \pm 0.017$ , while the  $I = 1$  parameter  $A_{I=1}$  increases from  $1.423 \pm 0.055$  to  $1.462 \pm 0.059$ . The interference term  $A_{int}$  is estimated as  $0.828 \pm 0.030$  and weakened. This value corresponds to a phase difference of  $\delta\theta_{I=0,1} = 34.1^{+3.0}_{-3.2}$ [degree] between the  $I = 0$  and  $I = 1$  interference terms. This is considered to be due to the increase in  $I = 1$ , which is primarily structured above the  $\bar{K}N$  threshold, being balanced by the intensity above the  $\bar{K}N$  threshold for  $I = 0$ .

Finally, there is room to further improve the fit by simultaneously fitting all parameters. The result is shown in Figure 4.24, where  $\chi^2/NDF = 184/41 = 4.48$ , and no significant improvement is observed. This suggests that  $A_{I=1}$  is determined from a single spectrum. Compared to the case where  $A_{I=1}$  was determined first, the parameters in this case show that  $A_{I=0}$  decreased from  $0.686 \pm 0.017$  to  $0.682 \pm 0.017$ ,  $A_{I=1}$  increased from  $1.462 \pm 0.059$  to  $1.570 \pm 0.058$ , and  $A_{int}$  decreased slightly from  $0.828 \pm 0.030$  to  $0.811 \pm 0.030$ , in the same direction as the introduction of  $A_{int}$ . This value of  $A_{int}$  corresponds to a phase  $\theta = 0.811 \pm 0.030$  shift.

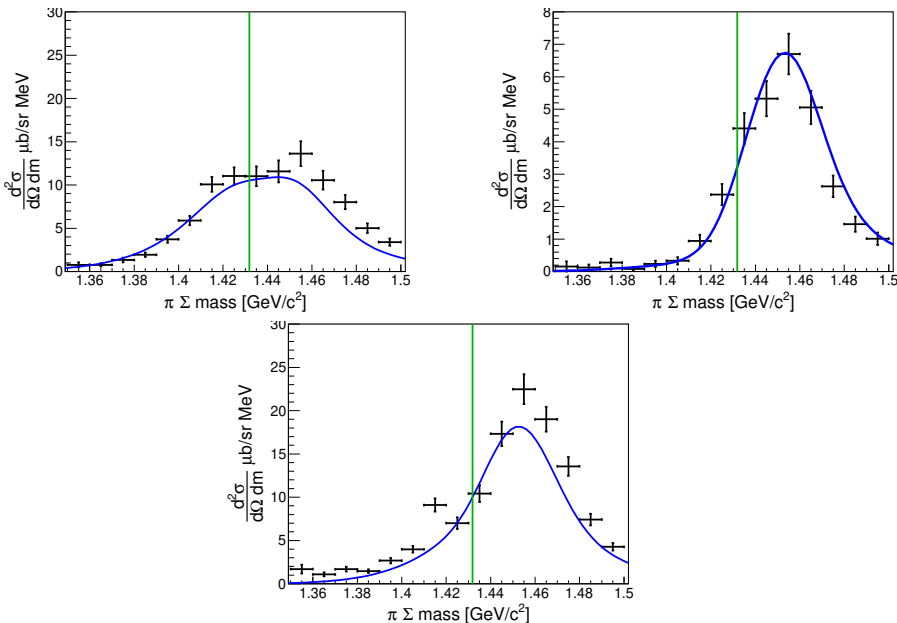


Figure 4.24: This figure shows the results of the fitting using Model.B with the introduction of parameters related to the interference term. The notation is the same as in Fig.4.22. All three parameters are determined simultaneously in this fitting.

# **Chapter 5**

# **Conclusion**

# **Appendix A**

## **$\pi^0\Sigma^0$ spectrum analysis**

# **Appendix B**

## **Detector resolution**

### **B.1 CDC resolution**

### **B.2 Detector resolution on the $d(K^-, N)$**

## Appendix C

### $d(K^-, n)K^0 n$ analysis

# Bibliography

- [1] R.L. Workman et al. (Particle Data Group), Prog. Theor. Exp. Phys. 2022, 083C01 (2022)  
"Review of Particle Physics"
- [2] R. H. Dalitz and A. Deloff, J. Phys. G17, 281 (1991).  
"The Shape and Parameters of the  $\Lambda(1405)$  Resonance"
- [3] M. Hassanvand et el., Phys. Rev. C **87**, 055202 (2013)  
"Theoretical analysis of  $\Lambda(1405) \rightarrow (\pi\Sigma)^0$  mass spectra produced in  $p + p \rightarrow p + \Lambda(1405) + p$  reactions"
- [4] J. Esmaili, Y. Akaishi, and T. Yamazaki, Phys. Lett. B **686**, 23 (2010)  
"Experimental confirmation of the  $\Lambda(1405)$  ansatz from resonant formation of a  $K^-p$  quasi-bound state in  $K^-$  absorption by  ${}^3\text{He}$  and  ${}^4\text{He}$ "
- [5] R. H. Dalitz and S. F. Tuan, Phys. Rev. Lett. 2 (1959).  
"Possible Resonant State in Pion-Hyperon Scattering"
- [6] M. H. Alston, L. W. Alvarez, P. Eberhard and M. L. Good, Phys. Rev. Lett. 6, 698 (1961).  
"Study of Resonances of the  $\Sigma$ - $\pi$  System"
- [7] R. J. Hemingway, Nucl Phys B **253**, 742 (1985).  
"Production of  $\Lambda(1405)$  in  $K^-p$  Reactions at  $4.2\text{GeV}/c$ "
- [8] B. Conforto et el., Nucl. Phys. B **34**, 41 (1971).  
"New experimental results on the Reactions  $K^-p \rightarrow \bar{K}N$  and  $K^-p \rightarrow \Sigma\pi$  a partial-wave analysis between 430 and  $800\text{MeV}/c$ "
- [9] A. J. Van Horn, Nucl. Phys. B **87**, 145 (1975).  
"Energy dependent partial-wave analysis of  $K^-p \rightarrow \Lambda\pi^0$  between 1540 and  $2215\text{MeV}$ "

- [10] R. J. Hemingway et el., Nucl. Phys. B **91**, 12 (1975).  
"New data on  $K^- p \rightarrow K^- p$  and  $K^0 n$  and a partial-wave analysis between 1840 and 2234MeV center of mass energy"
- [11] P. Baillon and P. J. Litchfield, Nucl. Phys. B **94**, 39 (1975).  
"Energy-independent partial-wave analysis of  $\bar{K}N \rightarrow \Lambda\pi$  between 1540 and 2150 MeV"
- [12] G. P. Gopal et al., Nucl. Phys. B **119**, 362 (1977).  
"Partial-wave analyses of KN two-body reactions between 1480 and 2170 MeV"
- [13] W. E. Humphrey and R. R. Rose, Phys. Rev. **127**, 1305(1962).  
"Low-Energy Interactions of  $K^-$  Mesons in Hydrogen"
- [14] J. K. Kim, Phys. Rev. Lett. **19**, 1074 (1967).  
"Multichannel Phase-Shift Analysis of  $\bar{K}N$  Interaction in the Region 0 to 550 MeV/c"
- [15] A. D. Martin, Nucl. Phys. B **179**, 33 (1981).  
"Kaon-Nucleon Parameters"
- [16] J. D. Davies et al., Phys. Lett. **83B**, 55 (1979).  
"Observation of kaonic hydrogen atom X-rays"
- [17] M. Izycki et al., Z. Phys. A **297**, 11 (1980).  
"Results of the search for  $K$ -series X-rays from kaonic hydrogen"
- [18] P. M. Bird et al., Nucl. Phys. A **404**, 482 (1983).  
"Kaonic Hydrogen atom X-rays"
- [19] M. Iwasaki et el., Phys. Rev. Lett. **78**, 3067 (1997).  
"Observation of Kaonic Hydrogen  $K_\alpha$  X Rays"
- [20] M. Bazzi et el., Phys. Lett. B **704**, 113 (2011).  
"A New Measurement of Kaonic Hydrogen X-Rays"
- [21] J.C.Nacher et el., Phys. Lett. B **455**, 55 (1999).  
"Photoproduction of the  $\Lambda(1405)$  on the proton and nuclei"
- [22] M. Niijima et el., Phys. Rev. C **78**, 035202 (2008).  
"Photoproduction of  $\Lambda(1405)$  and  $\Sigma(1385)$  on the proton at  $E_\gamma = 1.5$ - $2.4$ GeV/c"

- [23] K. Moria for the CLAS Collaboration, Phys. Rev. C **87**, 035206 (2013).  
"Measurement of the  $\pi\Sigma$  photoproduction line shapes near the  $\Lambda(1405)$ "
- [24] K. Moria for the CLAS Collaboration, Phys. Rev. Lett. **112**, 082004 (2014).  
"Spin and parity measurement of the  $\Lambda(1405)$  baryon"
- [25] S. X. Nakamura, and D. Jido, Prog. Theor. Exp. Phys., 023D01 (2014)  
"Lambda (1405) photoproduction based on the chiral unitary model"
- [26] D. Jido et al., Nucl. Phys. A **725**, 181 (2003).  
"Chiral Dynamics of the Two  $\Lambda(1405)$  States"
- [27] G. Agakishiev for the HADES Collaboration, Phys. Rev C **87**, 025201 (2013).  
"Baryonic Resonances to the  $\bar{K}N$  threshold: The case of  $\Lambda(1405)$  in  $pp$  collisions"
- [28] Y. Ikeda, T. Hyodo, and W. Weise, Nucl. Phys. A **881**, 98 (2012)  
"Chiral SU(3) theory of antikaon–nucleon interactions with improved threshold constraints"
- [29] Z.-H. Guo and J. Oller, Phys. Rev. C **87**, 3, 035202 (2013)  
"Meson-baryon reactions with strangeness - 1 within a chiral framework"
- [30] M. Mai and U.-G. Meißner, Eur. Phys. J. A **51**, 3, 30 (2015),  
"Constraints on the chiral unitary amplitude from  $\pi\Sigma K^+$  photoproduction data"
- [31] H. Zhang et al., Phys. Rev. C **88**, 035204 (2013).  
"Partial-wave analysis of  $\bar{K}N$  scattering reactions"
- [32] H. Zhang et al., Phys. Rev. C **88**, 035205 (2013).  
"Multichannel parametrization of  $\bar{K}N$  scattering amplitudes and extraction of resonance parameters"
- [33] H. Kamano et al., Phys. Rev. C **90**, 065202 (2014).  
"Dynamical Coupled-Channels Model of  $K^-p$  Reactions:  
Determination of Partial Wave Amplitudes"  
Phys. Rev. C **92**, 025205 (2015).  
"Dynamical Coupled-Channels Model of  $K^-p$  Reactions."

- Extraction of  $\Lambda^*$  and  $\Sigma^*$  Hyperon Resonances”  
 Phys. Rev. C**95**, 044903(E) (2015).
- [34] O. Braun et el., Nucl. Phys. B **129**, 1 (1977).  
 ”New Information About the Kaon-Nucleon-Hyperon Coupling Constants  $g(KN\Sigma(1197))$ ,  $g(KN\Sigma(1385))$  and  $g(KN\Lambda(1405))$ ”
- [35] D. Jido, E. Oset and T. Sekihara, Eur. Phys. J. A **42**, 257 (2009).  
 ”Kaonic Production of  $\Lambda(1405)$  off deuteron target in chiral dynamics”
- [36] J. Yamagata-Sekihara, T. Sekihara, and D. Jido, Prog. Theor. Exp. Phys. **2013**, 043D02 (2013).  
 ”Production of hyperon resonances induced by kaons on a deuteron target”
- [37] H. Noumi et el., Proposals for the 15th PAC meeting  
 ”Spectroscopic study of hyperon resonances below  $\bar{K}N$  threshold via the  $(K^-, n)$  reaction on Deuteron”
- [38] K. Miyagawa, J. Haidenbauer, and H. Kamada Phys. Rev. C **97**, 055209 (2018)  
 ”Faddev approach to the reaction  $K - d \rightarrow \pi\Sigma n$  at  $p_K = 1.0 GeV/c$ ”
- [39] E. Oset, A. Ramos, and C. Bennhold, Phys. Lett. B **527**, 99 (2002);  
**530**, 260(E) (2002).  
 ”Low lying  $S = -1$  excited baryons and chiral symmetry”
- [40] A. Cieplý and J. Smejkal, Nucl. Phys. A **881**, 115 (2012).  
 ”Chirally motivated  $\bar{K}N$  amplitudes for in-medium applications”
- [41] S. Ohnishi et el, Phys. Rev. C **93**, 025207 (2016).  
 ”Strcture of the  $\Lambda(1405)$  and the  $K^-d \rightarrow \pi\Sigma n$  reaction”
- [42] H. Kamano et el., Phys. ReV. C**94**, 065205 (2016).  
 ”Toward Establishing Low-Lying  $\Lambda$  and  $\Sigma$  Hyperon Resonances with the  $\bar{K} + d \rightarrow \pi + Y + N$  Reaction”
- [43] H. Noumi for the E31 Collaboration, Phys. ReV. B**837**, 137637 (2023).  
 ”Pole Position of  $\Lambda(1405)$  measured in  $d(K^-, n)\pi\Sigma$  reaction”
- [44] S. Kawasaki’s Doctor thesis will be submitted.
- [45] K. Agari et el, Prog. Theor. Exp. Phys., 02B009 (2012)

- [46] K. Agari et el, Prog. Theor. Exp. Phys., 02B011 (2012)
- [47] TRANSPORT <http://linac96.web.cern.ch/Linac96/Proceedings/Thursday/THP72/Paper.pdf>
- [48] T. K. Ohska et al., Nuclear Science, IEEE Transactions on **33**, 98 (1986).
- [49] M. Shiozawa and et el., A new TKO system manager board for a dead-time-free data acquisition system, in 1994 IEEE Nuclear Science Symposium-NSS'94, pages 632–635, (1994)
- [50] M. Iio et al., Nucl. Instrum. Methods Phys. Res., Sect. **A** **687**, 1 (2012).
- [51] S. Agostinelli et al., Nucl. Instrum. Methods Phys. Res., Sect. **A** **506**, 250 (2003)  
 J. Allison et al., IEEE Transactions on Phys. Sci. **53**, 207 (2006)  
 J. Allison et al., Nucl. Instrum. Methods Phys. Res., Sect. **A** **835**, 186 (2016)
- [52] K. Fuji, [https://www-jlc.kek.jp/subg/offl/lib/docs/helix\\_manip/node3.html](https://www-jlc.kek.jp/subg/offl/lib/docs/helix_manip/node3.html) (1968).
- [53] Opera Electromagnetic FEA Solution Software
- [54] V. Flaminio et al., CERN-HARA-87-01, 121 (1983).
- [55] M. Jones et el, Nucl. Phys. B **90**, 349 (1975)
- [56] R. Barlow and C. Beeston, Comp. Phys. Comm. **77**, 219 (1993).  
 "Fitting using finite Monte Carlo samples"
- [57] A. Nappi, Comp. Phys. Comm. **180**, 269 (2009).
- [58] C.J.S. Damerell et. el., Ncul. Phys. B**129**, 397 (1977). "  
 $K^-n$  elastic scattering between 610 and 840 MeV/ $c$ "
- [59] M. jones, R. Levi, Setti, D. Merrill and R. D. Tripp, Phys. Rev. B**90**, 349 (1975).  $K^-p$  charge exchange and hyperon production cross section from 860 to 1000 MeV/ $c$
- [60] M. Bernheim and et. el., Nucl. Phys. A**365**, 349, (1981). Momentum distributions of nucleons in the deuteron from  $d(e, e'p)n$  reaction
- [61] R. Machleidt, Phys. Rev. C**63**, 024001 (2001).
- [62] R. Barlow and C. Beeston, Comp. Phys. Comm. **77**, 219 (1993).

- [63] L. Lensniak, AIP Conf. Proc. 1030, 238–243 (2008). New formula for a resonant scattering near an inelastic threshold
- [64] S. Agostinelli et al., Nuclear Instruments and Methods in Physics Research Section A: Accelerators, Spectrometers, Detectors and Associated Equipment **506**, 250 (2003).  
J.Allison et el., Nuclear Instruments and Methods in Physics Research Section A: Accelerators, Spectrometers, Detectors and Associated Equipment **835**, 186 (2016).